Journal of Neuroscience Methods 242 (2015) 15–40

Contents lists available at ScienceDirect

Journal of Neuroscience Methods

journal homepage: www.elsevier.com/locate/jneumeth

Computational Neuroscience

Comprehensive chronic laminar single-unit, multi-unit, and local field potential recording performance with planar single shank electrode arrays

Takashi D.Y. Kozai[a,b,c,*], Zhanhong Du[a,b,c], Zhannetta V. Gugel[a,d], Matthew A. Smith[a,b,c,e], Steven M. Chase[b,f], Lance M. Bodily[g], Ellen M. Caparosa[g], Robert M. Friedlander[g], X. Tracy Cui[a,b,c]

[a] Bioengineering, University of Pittsburgh, United States
[b] Center for the Neural Basis of Cognition, United States
[c] McGowan Institute for Regenerative Medicine, University of Pittsburgh, United States
[d] Division of Biology and Biological Engineering, California Institute of Technology, United States
[e] Ophthalmology, University of Pittsburgh, United States
[f] Biomedical Engineering, Carnegie Mellon University, United States
[g] Neurological Surgery, University of Pittsburgh, United States

HIGHLIGHTS

- Established new methods for analyzing depth dependent recordings.
- Optimized novel metrics for quantifying evoked MU and LFP recording quality and stability.
- Neural recording of resting state underestimates the number of neurons available for recording.
- Depth of cortical layer IV can fluctuate in the 1st wk after implantation, but stabilizes after 2 wks.
- There is strong dependence on the biological layers of the cortex on chronic recordings.

ARTICLE INFO

Article history:
Received 8 October 2014
Received in revised form
11 December 2014
Accepted 15 December 2014
Available online 24 December 2014

Keywords:
Electrophysiology
Microelectrode arrays
Gamma oscillations
Firing rate
Power density spectra
Electrochemical impedance spectroscopy
Signal-to-noise
Visual evoked activity
Visual cortex

ABSTRACT

Background: Intracortical electrode arrays that can record extracellular action potentials from small, targeted groups of neurons are critical for basic neuroscience research and emerging clinical applications. In general, these electrode devices suffer from reliability and variability issues, which have led to comparative studies of existing and emerging electrode designs to optimize performance. Comparisons of different chronic recording devices have been limited to single-unit (SU) activity and employed a bulk averaging approach treating brain architecture as homogeneous with respect to electrode distribution.
New method: In this study, we optimize the methods and parameters to quantify evoked multi-unit (MU) and local field potential (LFP) recordings in eight mice visual cortices.
Results: These findings quantify the large recording differences stemming from anatomical differences in depth and the layer dependent relative changes to SU and MU recording performance over 6-months. For example, performance metrics in Layer V and stratum pyramidale were initially higher than Layer II/III, but decrease more rapidly. On the other hand, Layer II/III maintained recording metrics longer. In addition, chronic changes at the level of layer IV are evaluated using visually evoked current source density.
Comparison with existing method(s): The use of MU and LFP activity for evaluation and tracking biological depth provides a more comprehensive characterization of the electrophysiological performance landscape of microelectrodes.

* Corresponding author at: Department of Bioengineering, University of Pittsburgh, 5065 Biomedical Science Tower 3, 3501 Fifth Avenue, Pittsburgh, PA 15260, United States. Tel.: +1 4125438246.
E-mail addresses: tdk18@pitt.edu, tkozai@umich.edu (T.D.Y. Kozai).

http://dx.doi.org/10.1016/j.jneumeth.2014.12.010
0165-0270/© 2014 Elsevier B.V. All rights reserved.

Conclusions: A more extensive spatial and temporal insight into the chronic electrophysiological performance over time will help uncover the biological and mechanical failure mechanisms of the neural electrodes and direct future research toward the elucidation of design optimization for specific applications.

© 2014 Elsevier B.V. All rights reserved.

1. Introduction

Recent advances in brain–computer interfaces (BCIs) have demonstrated restoration of functional motor control in study participants with tetraplegia (Collinger et al., 2012; Simeral et al., 2011). These studies used penetrating intracortical electrodes as the critical front–end interface components for extracting the intent of tetraplegic patients through the firing rate of individual or small populations of neurons and the discrete location of the recording electrode over the motor cortex map. This intent can then be used to control robotic arms over multiple degrees of freedom. While these studies have increased enthusiasm in clinical application, such as treating tetraplegia, it should be noted that reliable chronic electrophysiological recordings also play a critical role in advancing our understanding of basic neuroscience such as behavior, decision-making, memory, plasticity, neural circuitry and connectivity (Gage et al., 2010; Ganguly and Carmena, 2009; Guitchounts et al., 2013; Richardson et al., 2012; Stoetzner et al., 2010). In addition, these electrodes are valuable tools in understanding the impact of neurological diseases and injuries.

1.1. Current neural interface challenges

The variability and long-term reliability issues of electrode recording performance have been well characterized in the literature (Kozai et al., 2010; Rousche and Normann, 1998; Williams et al., 1999) (see Kozai et al., 2015b for review). Electrophysiology and histology results show significant differences in recording performance and tissue integration with the same device across different animals, different electrode shanks in the same animal, and at different recording depths on the same shanks (Kozai et al., 2010; Rousche and Normann, 1998; Stensaas and Stensaas, 1976; Williams et al., 1999; Woolley et al., 2013). Regardless of the technology used, the electrophysiological performance degrades over time, which further translates to drop in unit yield over time (Barrese et al., 2013; Chestek et al., 2011; Kipke et al., 2008). The current challenge is to develop technology and methodology to reduce the variability and improve the reliability and stability of implantable neural interfaces (Bjornsson et al., 2006; Gilgunn et al., 2012; Johnson et al., 2007; Karumbaiah et al., 2013; Kolarcik et al., 2014; Kozai et al., 2014a, 2014b; Kozai and Kipke, 2009; Kozai et al., 2012a; Kozai et al., 2014c; Kozai et al., 2010; Potter et al., 2013; Potter et al., 2012; Sawyer and Kyriakides, 2013; Saxena et al., 2013; Winslow et al., 2010).

1.2. Approaches and limitations for understanding chronic failure mechanisms

To address challenges with variability and long-term stability, engineers have developed new technology and methodology across a wide design space including footprint size (Kozai et al., 2012a), electrode site size (Kozai et al., 2012a), volumetric density across the array's footprint, strength (Kozai et al., 2012a), compliance/flexibility (Kozai et al., 2012a), elasticity/softness (Harris et al., 2011), electrochemical properties (Cui et al., 2001; Cui and Martin, 2003a, 2003b), device insertion speed (Bjornsson et al., 2006; Johnson et al., 2007), tip shape (Bjornsson et al., 2006), and surface chemistry modifications, such as anti-biofouling (Kozai et al., 2012a), anti-inflammatory (Zhong and Bellamkonda, 2005), or neuron-specific adhesion molecule surfaces (Azemi et al., 2011; Kolarcik et al., 2012). However, current approaches to studying the long-term stability has led to limited understanding of the relationship between device design and chronic recording performance:

(1) Many of these studies examined the tissue response to non-functional electrodes, thus limiting the understanding of the impact of these designs on electrophysiology, especially since recent study has shown that histology is a poor predictor for electrophysiological performance (Kozai et al., 2014c).
(2) For studies that include functional electrodes with electrophysiological evaluation, there is often a disconnect between technologies developed by engineers and the performance needs of scientists. New and existing technologies are often compared without regard to the layer from which the recording sites reside (Karumbaiah et al., 2013; Ward et al., 2009), which greatly bias the results (Kozai et al., 2014c), and can be misleading for understanding device design.
(3) As the interface between biology and technology begin to blur through advanced surface chemistry (Kozai et al., 2012a), drug-release (Luo et al., 2011), substrate dissolution (Gilgunn et al., 2012; Kozai et al., 2014b), tissue integration (Azemi et al., 2011), and stem cell seeding (Azemi et al., 2010; Purcell et al., 2009), it is important to explore the impact of these biotic technologies on brain function and the functional neural network in the microenvironment surrounding the probe.
(4) While SU may be the most sensitive assay, not all studies and applications require the use of SUs. For example, MUs are more commonly used in human/primate BCIs (Chestek et al., 2011; Collinger et al., 2012; Fraser et al., 2009; Hochberg et al., 2012). Different research and neuroprosthetic applications require different designs optimized for collecting specific type of data (MU, LFP) and when performance is evaluated by SU alone, it can add to the complexity of attempting to extrapolate impactful information on how electrodes can be designed to record reliably for long periods of time within specific application needs.

To address all these issues, the functional MU and LFP recordings are assessed using evoked cues. Evaluation of neural recordings with new technologies requires careful consideration of animal models. In primate BCI studies, monkeys have been shown to alter their brain activity to compensate for the shortcomings of online decoding algorithms (Chase et al., 2009; Jarosiewicz et al., 2008). In essence, when using a decoding algorithm that misinterprets motor intent, primates can 're-aim', or alter their intent, to compensate (Chase et al., 2012). For the purposes of testing the functional performance of new technology, we feel it is best to simplify the experimental and animal model to minimize the subject's ability to alter intent, particularly when the subject is not capable of effectively communicating how the intent and online decoding algorithm deviate. Furthermore, it is impractical to test every new technology in primates. Lastly, moving animals generate a considerable amount of electromagnetic motion artifact as tissue moves along the electrode/cables or as the headstage cables move, making it difficult to distinguish between electromechanical noise and

multiunit activity (Ludwig et al., 2009; Shoham, 2003). In rodents, the motion artifacts generate spikes that have similar amplitudes, timescales, and waveforms to single-unit neural action potentials making them difficult to discriminate with principal component analysis (PCA). *To address these combined issues, we explore evoked electrophysiology in the mouse visual cortex for evaluating MU and LFP recording performance.* Mice have a large visual cortex that is easy to access, and their eyes remain open and fixed under anesthesia and awake head-fixed conditions (Sakatani and Isa, 2004). This eliminates the need to behaviorally train mice with reach tasks and removes the need to interpret the intent of a mouse. It further enables access to the large varieties of genetic toolboxes available to mice.

The goal of this study is to comprehensively optimize characterization methods for significant MU and LFP activity, and then compare their performance to SU performance. In this study, we characterize the longitudinal visually evoked electrophysiological performance of single shank planar Michigan electrodes chronically implanted into the visual cortex of mice. The study focuses on comparing the longitudinal SU and evoked electrophysiological recording characteristics along cortical layers of visual cortex and the underlying CA1 hippocampus. While spontaneous SU performance is easier to characterize and more commonly employed, visually evoked stimulation enables additional electrophysiological characterization of the recorded local field potentials (LFPs) and evoked spikes (single- & multi-unit) that are commonly used for many basic neuroscience research, primate research, and clinical applications (Chestek et al., 2011; Collinger et al., 2012; Flint et al., 2013; Fraser et al., 2009). The multitudes of analyses were employed to paint a more comprehensive picture of the electrophysiological performance landscape to provide new insight into a very complex implantable neural interface.

2. Methods

In the present study, we aim to comprehensively characterize the electrophysiological recording characteristics of chronically implanted penetrating cortical electrodes in the mouse along multiple layers of the cortex and hippocampus. Electrophysiological recording characteristics were evaluated across the metrics of SU yield, SU SNAR, SU amplitude, impedance, and noise floor as previously established (Kozai et al., 2012a). In addition, visually evoked MU and LFP activity were also evaluated using methods and metrics specifically developed for this study (see Sections 3.3–3.6 for details). Recording performance of electrodes was compared across 8 animals as well as across cortical and hippocampal depths. To compare across cortical depths, the depth of layer IV was first identified through current source density analysis (Smith et al., 2013; Stoelzel et al., 2009). Drifts in depths over time were evaluated, and then each array was aligned across animals to their most stable layer IV electrode position.

2.1. Surgery

Degeneratively doped silicon (.001 Ω-cm) 16 channel 3-mm long, base width of 123 μm, tapered single shank planar Michigan electrode with 703 μm^2 recording sites spaced 100 μm apart (A1 × 16-3 mm-100-703-CM16LP, Neuronexus Technologies. Ann Arbor, MI) were implanted into the left monocular visual cortex (1.0 mm anterior to lambda, 1.5 mm lateral from midline) of 9 week old C57BL/6 mice (22–28 g), because heavily doped silicon (0.1–0.01 Ω-cm) generated photoelectric artifact. All 8 subjects were induced with 1.5–2% isoflurane mixed with oxygen flow at 1 L/min, then maintained at 1.25–1.5%. After the animal was placed in a stereotaxic frame (Kopf Instruments, Tujunga, CA), the skin and connective tissue on the surface of the skull was removed. A thin layer of Vetbond (3 M) was placed over the skull. A small pinhole craniotomy was made over visual cortex with a high-speed dental drill and bone fragments were carefully removed with forceps and saline. Saline was applied continuously onto the skull to dissipate heat from the high-speed drill. Extra care was taken to prevent damage to the dura by reducing the drill speed and gently manually feeling the resistance of the skull when the dural blood vessels become visible through the opaque thin skull. Three bone screws were mounted on the skull, one over the contralateral visual cortex and two bilaterally over the motor cortex. The reference wire was tied to the ipsilateral motor cortex bone screw, and the preamplifier ground wire was shorted to the contralateral motor cortex and contralateral visual cortex bone screws. Stereotaxic insertion of the electrode was accomplished using a hand-driven micromanipulator at ~1 mm/s for 1.6 mm such that the top edge of the top recording site was at the surface of the brain. The final position of the electrode was carefully controlled by examining the electrode insertion site through a tilted surgical scope. The electrode was inserted with the recording sites facing laterally (i.e. away from the midline, and toward V1m/V1b).

After insertion, the craniotomy was filled and the silicon electrode was protected using nontoxic silicone elastomer (Kwik-sil, World Precision Instruments) (Azemi et al., 2011; Guitchounts et al., 2013; Kozai et al., 2012a; Scott et al., 2012), which has been shown to have good biocompatibility with the brain and no observable influence on brain swelling or shrinkage. The electrode and bone screws were then cemented into place with dental cement (Pentron Clinical, Orange, CA). Animal temperature was maintained throughout the procedure using a warm water pad (HTP 1500, Adroit Medical Systems, Loudon TN). After the ~45 min procedure, a 3 cc injection of sterile 37° Ringer's solution was given subcutaneously to the back of the animal to aid recovery. Buprenorphine (0.3 mg/kg) was administered twice daily for three days as a postoperative analgesic. All experimental protocols were approved by the University of Pittsburgh's Institutional Animal Care and Use Committee.

2.2. Neurophysiological recording

Electrophysiological recordings were taken from the animal inside of a faraday cage with a visual stimulus-presenting computer monitor located outside of the cage (Fig. 1a and b) (Brainard, 1997; Cornelissen et al., 2002; Kleiner et al., 2007). 130 s of spontaneous (resting state) and visually evoked signals from the electrodes were sampled at 24,414 Hz. During each recording session, animals were situated on a microwaveable heating pad (Deltaphase isothermal pad, Braintree Scientific, Inc, Braintree, MA) inside of a darkened faraday cage (1.6 mm mesh) while lightly anesthetized with isoflurane (Fig. 1a and b). The faraday cage mesh size blocked major environmental noise (e.g. 60 Hz) without substantially blocking light from the monitor, which was placed just outside of the cage. The cage was grounded, but otherwise electrically isolated. Electrophysiological data was transferred outside of the cage through a nonconductive optic fiber via a battery-powered preamplifier (Medusa preamp, Tucker-Davis Technologies, Alachua, FL) housed inside of the faraday cage using previously published methods (Kozai et al., 2012a). Inputs and outputs from the cage were limited to gas or optical (Kozai et al., 2012a).

A 24″ LCD screen (V243H, Acer. Xizhi, New Taipei City, Taiwan) was positioned outside of the cage and the animal's head was mechanically fixed to the induction box through a custom built holder and placed 20 cm from the contralateral eye of implantation spanning a total visual field of 120° wide by 60° high. Resting state recording was conducted in a dark room with the monitor turned off. To evoke activity in the visual cortex, visual

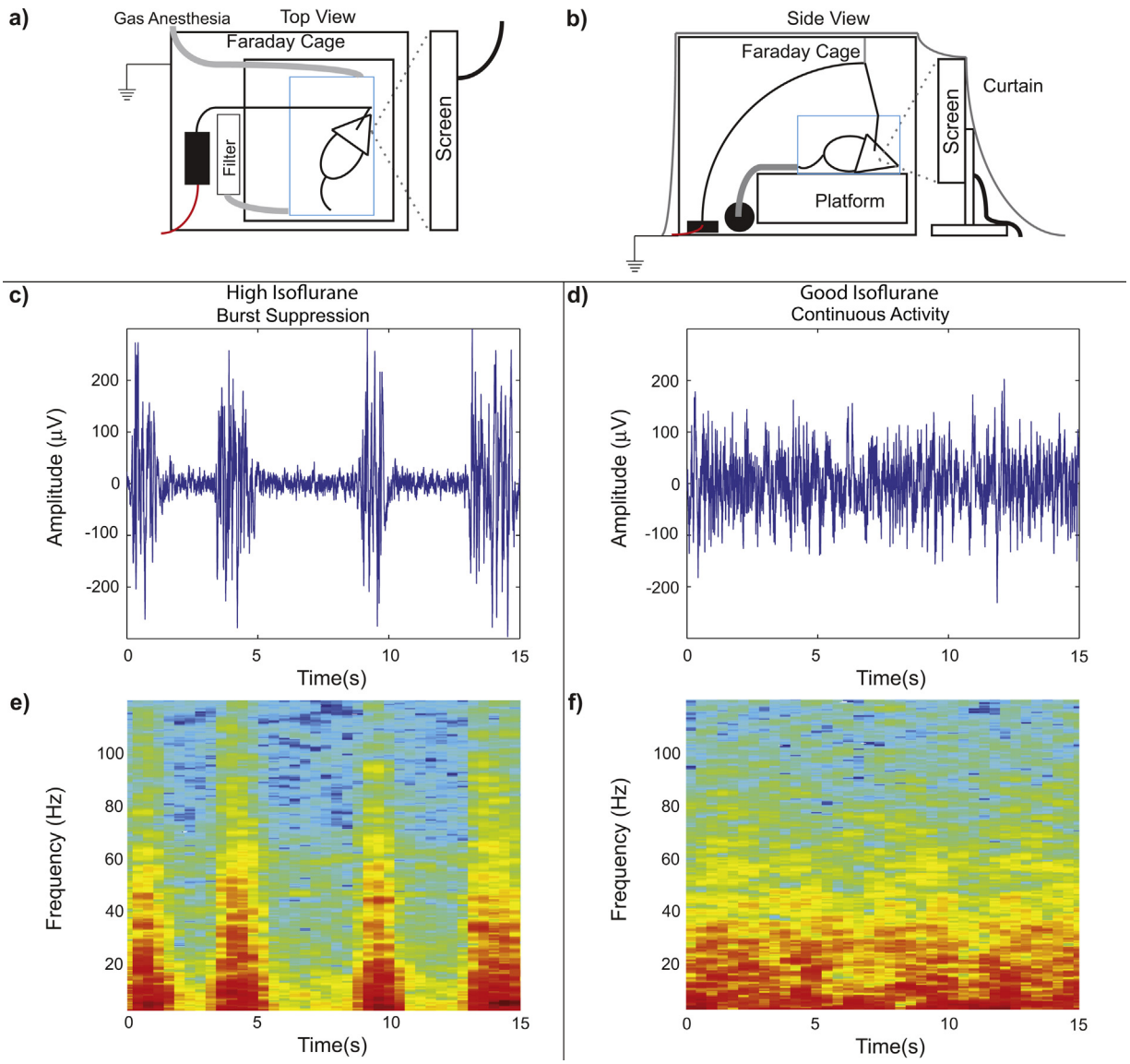

Fig. 1. Experimental setup. (a) and (b) Blue box is a transparent isoflurane induction box. Red indicates an optic data cable. (c)–(f) Isofluorane level was calibrated so that the animals remain immobile, but burst suppression activity (c) and (e) was eliminated and continuous brain activity (d) and (f) could be detected in the LFP and wideband electrophysiological streams. (c)–(d) LFP (2–300 Hz). (e) and (f) LFP spectrogram (2–120 Hz). (c) and (e) and (d) and (f) are from the same animal <2 min apart. (For interpretation of the references to color in this figure legend, the reader is referred to the web version of this article.)

stimuli were presented using the MATLAB-based Psychophysics Toolbox (Psychtoolbox) (Brainard, 1997; Kleiner et al., 2007; Pelli, 1997). Full-field solid black and white bar gratings were presented drifting in a perpendicular or 45° directions. Using Psychtoolbox, the timing of the visual stimulation was synchronized with the recording system (RX5, Tucker-Davis Technologies, Alachua FL) via transistor-transistor logic (TTL) pulses sent from the display computer through a stimulus isolator (A-M Systems Model 2200). Drifting gratings were presented for 1 or 4 s followed by an equal duration dark screen period.

Animal anesthesia level was set at the lowest concentration sufficient for the maintenance of animal inactivity (0.75–1.1%). Subjects were carefully observed during recording to ensure that the proper level of anesthesia (stage 3-plane1) was maintained. Proper level of anesthesia is defined as the lowest anesthesia concentration sufficient for maintaining animal inactivity while avoiding synchronous bursting neural activity (Fig. 1c–f) as synchronous bursting (or burst suppression) leads to poor evoked neural activity and synaptic transmission (Goncalves et al., 2013; Hudson et al., 2014; Mukamel et al., 2014). For the first week following surgery, while the animal was recovering from surgery and under the influence of analgesics, low anesthesia levels were necessary to maintain animal inactivity (0.75–1.0%). Starting the second week, anesthesia levels of 1.1% were needed to maintain inactivity and still evoke neural activity.

2.3. Electrophysiological signal processing

The raw data stream was filtered to produce LFP (1–300 Hz) and spike (300–5000 Hz) data streams (Fig. 2). The spike data stream was further pre-processed using the previously published common average referencing method (Kozai et al., 2012a; Ludwig et al., 2009). To identify individual units, the threshold for the high-frequency data was established by using a window set at 3.5 standard deviations below the mean of the data (Kozai et al., 2012a; Ludwig et al., 2009).

For the purposes of this manuscript, the following definitions are used: (1) Single-unit activity is defined as the activity

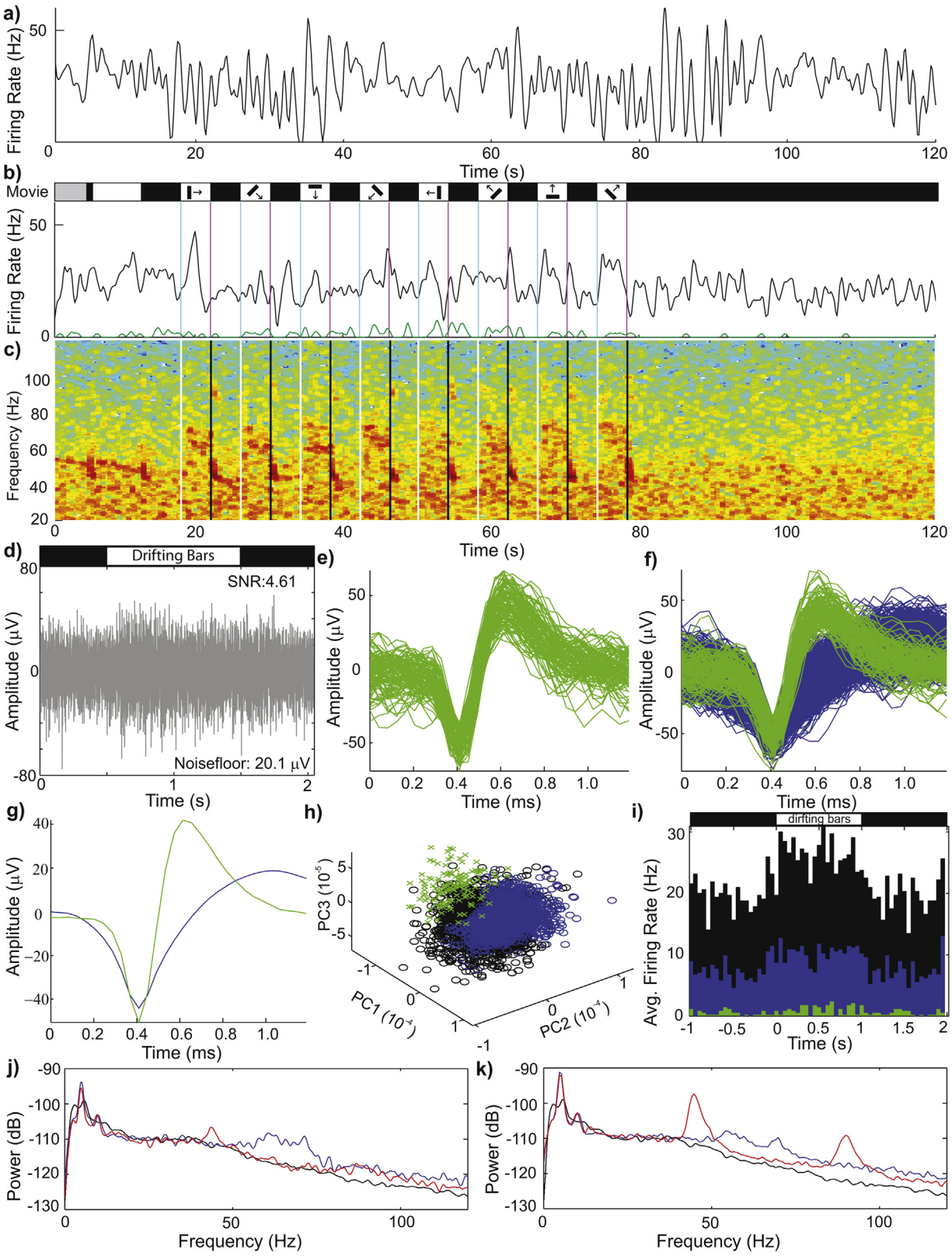

Fig. 2. Example resting state and evoked recording session 2 months post-implant from one animal. (a) Example channel of dark room spontaneous "resting state" recording showing the firing rate of only the unsorted outlier after automated spike sorting (multiunit: black). (b) Same as (a) except visually evoked with a drifting grating movie. Auto-spike sorting discriminated a high amplitude, low firing SU (green) which increased firing rate during the visual stimulus. *Note*: First 15 s are movie calibration. (c) LFP spectrogram from the same session. Strong activation can be observed around ~70 Hz during the 'ON' stimulus, and at ~45 Hz and ~90 Hz briefly after the stimulus ends. (d) Raw spike channel (300–5000 Hz) show increased spiking during the 'ON' stimulus. (e) SU from (b) sorted with automated sorting during 8 × 4 s × 1 cycle stimulus (46.1 spikes/min). (f) Two distinct SUs sorted by 8 × 1 s × 8 cycle stimulus (51.3 & 478.9 spikes/min). (g) Mean waveform of (f). (h) PCA cluster of (f). (i) PSTH of (d), (f) showing increased firing during the 'ON' stimulus (multiunit: black). (j) LFP Power Density Spectrum during the 4 s stimulus showing increased power ~70 Hz during 'ON' (blue) and ~45 Hz during 'OFF' (red), compared to resting state (black). (k) Same as (j) for 1 s stimulus showing stronger activation. (For interpretation of the references to color in this figure legend, the reader is referred to the web version of this article.)

of a single neuron as distinguishable by PCA. (2) Outlier cluster activity is defined as the activity of the unsorted, outlier threshold-crossing events as defined by offline sorting (i.e., all the waveforms that exceeded threshold but did not belong to well-defined SUs). Because environmental noise and motion artifacts have been minimized through experimental setup, a majority of these events are of neural origin. (3) MU activity is defined as the activity of all threshold-crossing events containing both sorted single-unit activity and outlier cluster activity.

2.4. SU analysis

Offline spike sorting was carried out using a custom MATLAB script described below. A 1.2 ms waveform snippet was extracted on threshold crossings from the spike data stream. To isolate single neuronal units, the first 6 principal components (PCs) were calculated from the waveforms. The resultant components were used to separate the waveforms into individual clusters by a previously published automatic spike sorting method (Bokil et al., 2010; Fee et al., 1996) in the Chronux toolbox. The SU signal quality was defined as signal-to-noise amplitude ratio (SNAR), and was calculated as the peak-to-peak amplitude of the mean waveform of the cluster divided by twice the standard deviation of the noise:

$$SU\ SNAR = \frac{\mu_{SU-pp}}{2\sigma_N} \quad (1)$$

where $\mu_{SU\text{-}pp}$ is the mean peak-to-peak amplitude of the waveform snippets and σ_N is the standard deviation of the spike data stream *after* all waveform snippets have been removed. If no single unit was detected, SNAR was considered to be 0, unless otherwise stated, for the purposes of calculating average signal amplitude and SNAR.

Candidate units with SNAR between 2 and 3 were manually confirmed or excluded by examining the combination of waveform shape, auto-correlogram, peak threshold crossing offset, and peri-stimulus time histogram (PSTH) with 50 ms bins. Candidate units with SNAR below 2 were discarded, and candidate units with SNAR greater than 3 were manually confirmed by examining the waveform shape.

2.5. Multi-unit (MU) analysis

Using a photo-detecting diode connected to a separate RX5 analog input, the hardware & software delay for Psychophysics toolbox was measured, and the TTL trigger was realigned to the onset of the image on the computer screen. The threshold crossing multiunit PSTH of the visual stimulation trigger is calculated for each channel. To compute the evoked MU yield for our electrodes, we compared the MU spike count from a 550 ms wide bin starting 50 ms after stimulus onset to the number of spikes in a 550 ms bin ending 50 ms before stimulus onset (Fig. 3). Channels with significantly different visually evoked MU activity between the two epochs ($p < .05$ as assessed with a paired t-test) were reported in MU yield. The 550 ms bin size was chosen by comparing all possible bin widths from 50 ms to 1000 ms (in 50 ms increments); 550 ms was found to maximize MU yield (Fig. 3c and d). Similarly, the +50 ms latency was determined by comparing −50 ms, +0 ms, +50 ms, +100 ms, or +150 ms shift from the visual trigger for maximum yield (Fig. 3c and d). Latencies were examined by applying the delay to both 'ON' and 'OFF' bins as well as applying the delay solely to the 'ON' bin while locking the 'OFF' state to the visual trigger. While this may not detect channels that are recording MUs with very small firing rate changes, it is a conservative method for identifying channels recording information encoded units.

While SU signal strength can be quantified as the average voltage amplitude of the largest sorted single unit, threshold-crossing events which include MU were a mixture of possible SUs with various amplitudes. Therefore MU signal strength of the largest reliable MU amplitude was estimated using the quality metric defined as

$$MU\ Amplitude = \mu_{MU-pp} + 2\sigma_{MU-pp} \quad (2)$$

where $\mu_{MU\text{-}pp}$ and $\sigma_{MU\text{-}pp}$ are the mean peak-to-peak amplitude of all MUs and standard deviation of all of the waveform snippets, respectively. That is, the strength of the multiunit signal is defined as the average peak-to-peak MU amplitude plus two standard deviations of the standard deviation of all MU peak-to-peak amplitude. We further quantified MU signal quality by defining the Signal-to-Noise Firing Rate Ratio (SNFRR) for MU as the average firing rate of the 'ON' state minus the average firing rate of the 'OFF' state divided by the average standard deviation of both the 'ON' and 'OFF' state.

$$MU\ SNFRR_{ON:OFF} = \frac{\mu_{on} - \mu_{off}}{1/2(\sigma_{on} + \sigma_{off})} \quad (3)$$

where μ_{on} and μ_{off} are the mean MU firing rate of the 'ON' and 'OFF' state, respectively, while σ_{on} and σ_{off} are the standard deviation of firing rates during the 'ON' or 'OFF' state, respectively. Two-sided Welch's t-test with the assumption of unequal variance and a p-value < 0.05 was conducted between 'ON' and 'OFF' firing rates. If no significant multi-unit was detected, MU amplitude and SNFRR were considered to be 0, unless otherwise stated, for the purposes of calculating average signal amplitude and SNFRR. For depth vs time figures, MU data was also evaluated using a conservative Bonferroni correction to account for multiple comparisons ($p < 0.05$, $\alpha < 1.645 \times 10^{-5}$: See supplementary information).

2.6. Local field potential analysis

LFP analysis was carried out with a custom MATLAB script based on a previously published method (Bokil et al., 2010) in the Chronux toolbox. Briefly, a Butterworth filter at 2–300 Hz is applied to raw data to obtain the LFP signal. Multi taper methods are utilized to estimate LFP power spectrum and spectrograms. For the power spectrum, a time-bandwidth product of 1 and a taper number of 1 is utilized for multi-taper estimation; for LFP spectrogram, a moving window of 2 s duration and 0.4 s step is chosen, with a time-bandwidth product of 5 and the taper number of 2 for multi-taper estimation.

Various methodologies to quantify and analyze LFPs in the literature were explored to determine the method that yielded the greatest amount of significant recordings (Burns et al., 2010; Buzsaki et al., 2012; Jia et al., 2011; Land et al., 2013b; Sellers et al., 2013; Spaak et al., 2012; Vazquez et al., 2013; Xing et al., 2012). LFP data were compared to the resting state data corresponding to the same imaging session of the same animal on each recording day. To obtain unbiased normalizations of the LFP ON and OFF evoked responses, the resting state LFP activity was pseudo-triggered to ON and OFF responses. The triggers mimicked the timing of the movie used for evoked stimulation.

2.6.1. Evoked LFP voltage response

The transient evoked LFP voltage responses were found by:

$$LFP_{v+} = \max(LFP_v) \quad (4)$$

$$LFP_{v-} = \min(LFP_v) \quad (5)$$

$$LFP_{v\pm} = \max(LFP_v) + |\min(LFP_v)| \quad (6)$$

where LFP_{v+} is the maximum (positive) amplitude, LFP_{v-} is the minimum (negative) amplitude, and $LFP_{v\pm}$ is the peak-to-peak amplitude of the LFP data stream (LFP_v) within the first 1000 ms following the stimulus trigger as previously established (Land et al., 2013b; Vazquez et al., 2013).

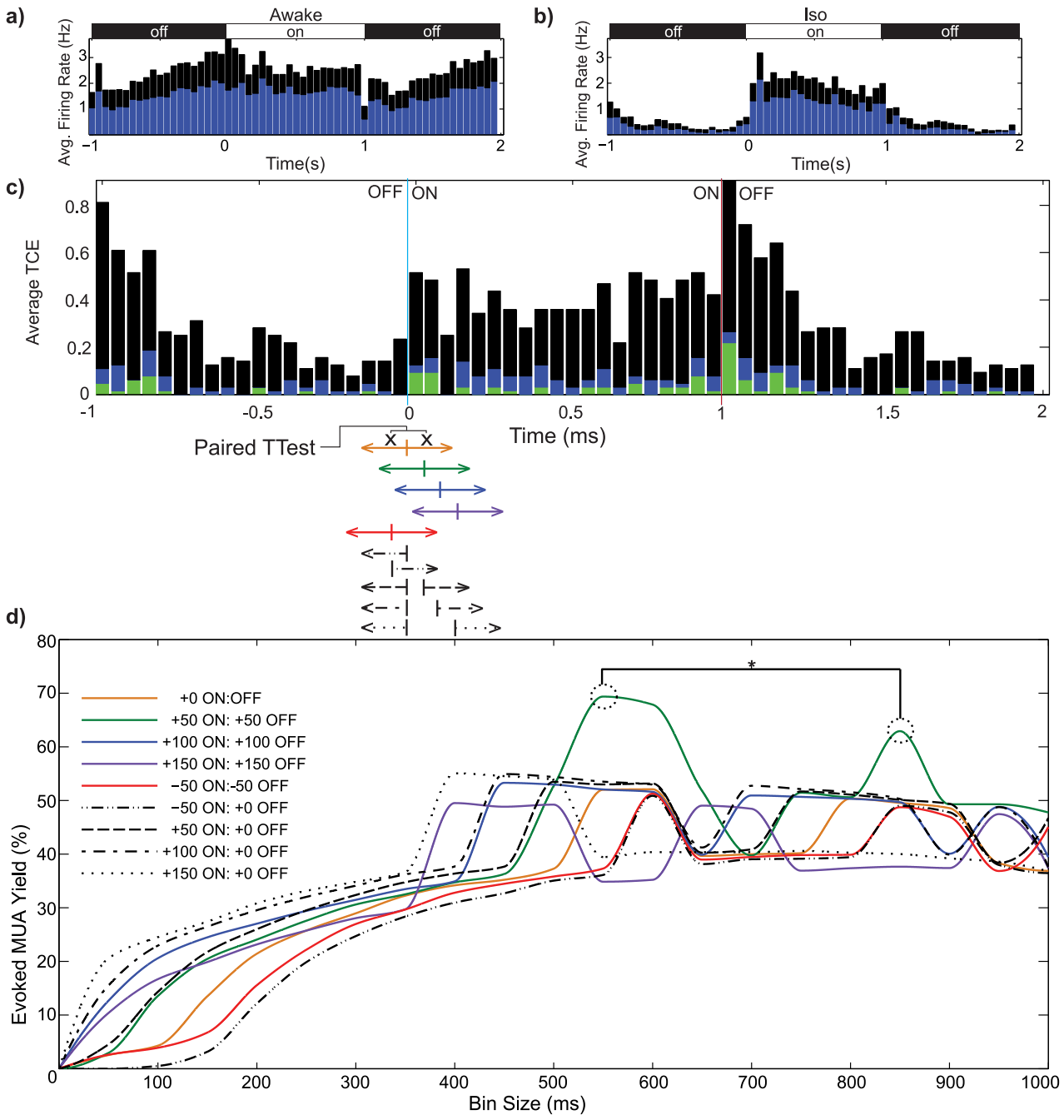

Fig. 3. Evoked multi-unit activity optimization. (a) PSTH of from the same mouse under awake head-fixed and (b) anesthetized head-fixed conditions. Under awake head-fixed condition, there is greater basal firing rate activity compared to anesthetized. Therefore, for the purposes of quantifying MUA Yield, anesthetized condition can be better for detecting significant evoked activity. (c) PSTH of showing increased firing during the 'ON' stimulus. Different colors and line types illustrate corresponding bin size delays and offsets of the bin size for (d). (d) MU yield evaluated with *t*-test of number of threshold crossings before and after the stimulus. A 550 ms bin before and after a +50 ms latency delay from the initial stimulus shows the greatest yield. These conditions are used for MUA analysis for the remainder of this study. (For interpretation of the references to color in this figure legend, the reader is referred to the web version of this article.)

Previous studies have also evaluated evoked voltage area (Land et al., 2013b; Spaak et al., 2012). Expanding upon these studies, the positive and negative voltage area were calculated to quantify total resonance in the signal (Buzsaki et al., 2012).

$$LFP_{\sum v+} = \int_t LFP_v \cdot dt,\ [t|LFP_v(t) > 0] \tag{7}$$

$$LFP_{\sum v-} = \int_t LFP_v \cdot dt,\ [t|LFP_v(t) < 0] \tag{8}$$

$$LFP_{\sum v\pm} = \int_t |LFP_v| \cdot dt \tag{9}$$

where $LFP_{\Sigma v+}$ is the positive voltage area, $LFP_{\Sigma v-}$ is the negative voltage area, LFP_v is LFP voltage, $LFP_{\Sigma v\pm}$ describes the total (positive and negative) fluctuations of LFP, and t is time from 0 to 1000 ms as established previously (Land et al., 2013b) to capture the transient and sustained LFP voltage activity (Xing et al., 2012).

2.6.2. Evoked LFP power response

Evoked LFP voltage deflections can greatly depend on the layer recorded (Fig. 7a and b). The border between Layer IV and V and in the callosum, the evoked voltage amplitude can be smaller than other layers. Therefore, the LFP power spectrum was also examined as LFP quantification metrics. LFP power (*LFPp*) was computed by passing raw voltage ON, OFF and pseudo-triggered resting state activity into *mtspectrumc.m* in the Chronux toolbox. The parameters used include 5 and 9 for tapers, sampling rate of 2441, zero padding and cut-off frequency between 0 and 125 Hz. LFP power was transformed into power in decibels (dB) by calculating the base 10 logarithm of the ON and OFF voltage waveforms. Power in the gamma band (20–120 Hz) was analyzed due to its high information content in evoked visual cortex. To allow for statistical comparison of evoked LFPs (ON and OFF) with resting state LFPs ($RSp_{pseudoON}$ and $RSp_{pseudoOFF}$), the evoked and resting state activity were normalized. Normalization was conducted via subtraction or division by the resting state LFP power spectrum, and then offset so that resting state activity is defined as zero as previously established (Jia et al., 2011; Xing et al., 2012):

$$LFPp_{E-RS} = Evoked_E - \frac{(RSp_{pseudoON} + RSp_{pseudoOFFN})}{2} \quad (10)$$

$$LFPp_{E:RS} = \frac{Evoked_E}{1/2(RSp_{pseudoON} + RSp_{pseudoOFF})} - 1 \quad (11)$$

where $Evoked_E$ is power spectrum of the visually evoked LFP ($Evoked_{ON}$ or $Evoked_{OFF}$), $RS_{pseudoON}$ is the power spectrum of the pseudo-triggered ON resting state, and $RS_{pseudoOFF}$ is the power spectrum of the pseudo-triggered OFF resting state. This normalization flattens the LFP power across all frequency and highlights the evoked LFP power feature in a frequency independent manner. Because power generally decreases with increase in frequency, dividing by resting state more favorably weighs higher frequency gamma activity compared to subtraction. Evoked power was also normalized directly between $Evoked_{ON}$ and $Evoked_{OFF}$:

$$LFPp_{ON-OFF} = Evoked_{ON} - Evoked_{OFF} \quad (12)$$

$$LFPp_{ON:OFF} = \frac{Evoked_{ON}}{Evoked_{OFF}} - 1 \quad (13)$$

For each normalized response, the mean and median of the resting state ($RSp_{pseudoON}$ and $RSp_{pseudoOFF}$) and evoked ($Evoked_E$: $Evoked_{ON}$ or $Evoked_{OFF}$) responses were calculated across gamma frequencies (20–120 Hz) for recording channel (Jia et al., 2011; Sellers et al., 2013).

Because evoked gamma oscillation frequencies can vary between animal and cortical location, peak power was also evaluated for quantifying frequency independent evoked activity (Burns et al., 2010). Peak analysis was applied using:

$$LFPp_{ppE-RS} = \max(LFPp_{E-RS}) - \min(LFPp_{E-RS}) \quad (14)$$

$$LFPp_{ppON-OFF} = \max(LFP_{ON} - LFP_{OFF}) - \min(LFP_{ON} - LFP_{OFF}) \quad (15)$$

where $LFPp_{ppE\text{-}RS}$ is the peak-to-peak power of the normalized evoked ON or OFF LFP activity, and $LFPp_{ppON\text{-}OFF}$ is the peak-to-peak power between LFP_{ON} *and* LFP_{OFF}.

2.6.3. Significant evoked LFP activity

Resting state and evoked responses were statistically compared with each technique listed in Eqs. (4)–(15) above using a two-sided Welch's *t*-test with the assumption of unequal variance and a *p*-value <0.05 considered significant (see Table 1 for a summary of all statistical tests conducted).

To determine the most efficient method of LFP analysis, the total average yield across all animals and recording days was calculated. Because the LFP signal can be influenced by common ECoG signals from the contralateral reference bone screw, common average referencing (CAR) was also explored to examine unique LFP signals in the local neuronal network around the array (Ludwig et al., 2009). Briefly, CAR was found by averaging the raw signal from all channels for each trial and then subtracting the average signal from each channel. None of the channels experienced preamplifier saturation (or railing/clipping), so no channels were manually removed from CAR. The signals were analyzed using the Chronux toolbox as described earlier in *Methods*, and LFP voltage and power were analyzed according to Eqs. (4)–(15) above. The most efficient method which produces the statistically largest overall LFP yield was the $LFPp_{ppE\text{-}RS}$. This method was then applied to all subsequent analyses of LFP including stability, signal strength, and SNLPR of the ON and OFF responses unless stated otherwise.

2.6.4. LFP quality

Signal quality was quantified for significant evoked LFP responses compared to resting state activity. The maximum normalized CAR LFP ON power peak of the evoked LFP response was found across V1 lamina and averaged across animals for each recording day. Channels lacking significant differences from resting state data were assigned a peak value of zero. The signal-to-noise LFP power response ratio (SNLPR) is calculated according to Eq. (14):

$$SNLPR = \frac{\mu(\max(LFPp_{ON=RS}))}{\sigma(1/2(LFP_{pseudo\,ON-RS} + LFP_{pseudo\,OFF-RS}))} \quad (16)$$

where the trial-averaged peak (maximum) of the ON response (normalized by Eq. (10)) is divided by the standard deviation of the mean normalized resting state.

2.6.5. LFP stability

The LFP power spectra showed that the evoked power peak frequency bands are conserved along the lamina and across time (Fig. 4e–h), though the peak frequencies can differ between animals and implant locations (Fig. S2). Stability of the CAR LFP ON power peak frequency was quantified by calculating the frequency shift in significant peaks of the power profile over time. The frequency at which the maximum peak occurs was found and stored for each day per animal. Frequency shift was quantified by:

$$f_s(d) = \left|\rho_f(d) - \rho_{f,i}\right| \quad (17)$$

where f_s is frequency shift in Hz, d is days, ρ_f is the peak frequency and $\rho_{f,I}$ is the initial peak frequency. The initial peak frequency is the first recording session containing a significant peak (compared to resting state peak). The absolute value of the difference was found to avoid potential cancelations when averaging across animals. Frequency shift was averaged across animals and displayed across laminar depth and recording days.

2.7. Current source density

Current source density (CSD) analysis was employed to identify the depth of Layer IV. CSD was performed by computing the average evoked (stimulus-locked) LFP at each site, and then calculating the second spatial derivative (Smith et al., 2013; Stoelzel et al., 2009). We averaged the CSDs across 64 stimulus trials and determined the input layer (IV) as the depth at which the minimum value of the CSD occured in the first 100 ms. Polarity inversion of LFP was also examined to supplement the CSD analysis (Yazdan-Shahmorad et al., 2011). Layer IV was examined to study the changes of electrode depth over time and to align recording data across animals to a common Layer IV.

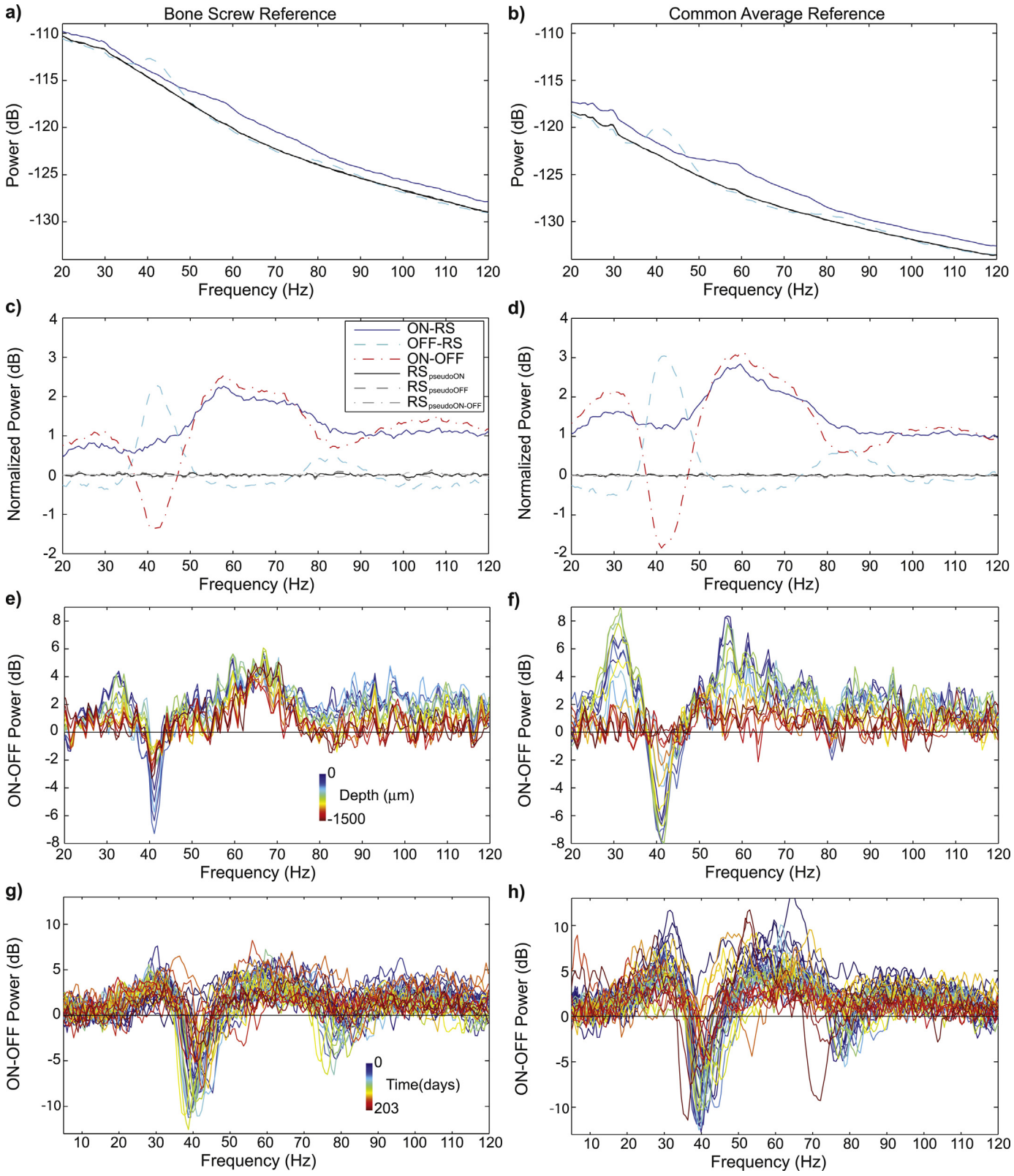

Fig. 4. Evoked local field potential power quantification using the bone screw reference (a), (c), (e), (g) and CAR (b), (d), (f), (h). In general, CAR better separates evoked LFP power compared to resting state activity than contralateral bone screw reference. (a) and (b) Non-normalized γ-LFP power averaged across depth, days and animals. Shown is the γ-LFP ON response (blue), OFF (red) and pseudo triggered resting state ON (gray) and resting state OFF (black dashes). (c) and (d) Power responses were normalized by resting state subtraction (Eq. (10)) to allow for quantification of peaks and area of each profile. Shown is the γ-LFP ON response (solid blue), OFF (dashed cyan), ON-OFF (dash dot red), Resting $State_{pseudoON}$ (solid black), Resting $State_{pseudoOFF}$ (dashed gray) and Resting $State_{pseudoON\text{-}OFF}$ (dashed dot silver). For each dataset, normalized profiles were calculated and utilized for yield, SNLPR, yield, strength, and steadiness analysis of γ-LFP. (e) and (f) Peak/Valley is conserved across depth although the peak power is affected by depth. (g) and (h) Peak/Valley is conserved across days. (For interpretation of the references to color in this figure legend, the reader is referred to the web version of this article.)

Table 1
LFP statistic methods.

VOLTAGE STATISTICS: positive, negative, and total Voltage Amplitude & Area (Eqs. (4)–(9))	LFP_{v+}		*T*-test VS
	LFP_{v-}		
	$LFP_{v-\pm}$		
	$LFP_{\Sigma v+}$	ON	$RSv_{pseudoON}$
	$LFP_{\Sigma v-}$	OFF	$RSv_{pseudoOFF}$
	$LFP_{\Sigma v-\pm}$	|ON| + |OFF|	$\lvert RSv_{pseudoON}\rvert + \lvert RSv_{pseudoOFF}\rvert$
POWER STATISTICS: Mean and Median Normalized Power (Eqs. (10)–(13))			*T*-test VS
		ON	$RSp_{pseudoON}$
	$LFPp_{E\text{-}RS}$	OFF	$RSp_{pseudoOFF}$
	$LFPp_{E:RS}$	|ON-OFF|	$\lvert RSp_{pseudoON} - RSp_{pseudoOFF}\rvert$
	$LFPp_{ON:OFF}$	ON	OFF
Peak POWER Normalized Power (Eqs. (14) and (15))			*T*-test VS
		ON	$RSp_{pseudoON}$
	$LFPp_{ppE\text{-}RS}$	OFF	$RSp_{pseudoOFF}$
	$LFPp_{ppON\text{-}OFF}$	|ON-OFF|	$\lvert RSp_{pseudoON} - RSp_{pseudoOFF}\rvert$

2.8. Impedance spectroscopy

Electrochemical impedance was measured immediately after each neural recording session. While under anesthesia, the implanted array was connected to an Autolab potentiostat using a 16 channel multiplexer. Impedance was measured for each channel using a 10 mV RMS sine wave from 10 Hz to 32 kHz, employing a 15 multisine paradigm to shorten the time required for measurement. In this work, the 1 kHz impedance is reported unless indicated otherwise.

2.9. Immunohistochemistry

Animals were sacrificed and perfused according to University of Pittsburgh IACUC approved methods. Each animal was deeply anesthetized using a 90 mg/kg ketamine, 9 mg/kg xylazine cocktail. Once the proper plane of anesthesia was observed, animals were transcardially perfused using a warm 1xPBS flush at ~70 mmHg followed by ice cold 4% paraformaldehyde at 70–90 mmHg. Animals were decapitated, and heads were post-fixed in a 4% paraformaldehyde bath at 4 °C for 4–6 h. Skulls with the headcap and brain were then removed and soaked in a 15% sucrose bath at 4 °C overnight followed by a 30% sucrose bath for 36–48 h. Following the sucrose protection, the bottom and sides of the skull was carefully dissected without damaging the brain using microscissors and forceps. Then tweezers were used to gently lift the brain from the electrode array and headcap. Brains were then blocked and carefully frozen in a 2:1 20% sucrose in 1xPBS:optimal cutting temperature compound (Tissue-Tek, Miles Inc., Elkhart, IN) blend with dry ice. Tissue was coronally or horizontally sectioned using a 25 μm slice thickness using a cryostat (CM1950 Leica, Buffalo Grove, IL).

Tissue sections were rehydrated with 5 min washes with 1× phosphate buffer saline (PBS), repeated twice. The tissues were then incubated in a humidified chamber with pH 6.0, 0.01 M sodium citrate buffer for 30 min at 60 °C. Then, a peroxidase block was performed in 1× PBS with 10% v/v methanol and 3% v/v hydrogen peroxide for 20 min on a table shaker. Next, tissue sections were incubated in a blocking solution (5% goat serum, 0.1% triton X-100) for 30 min at room temperature. Lastly, the tissue samples were blocked with 0.1 mg/ml AffiniPure Fab Fragment (Alexa-647 115–607-003 Jackson ImmunoResearch Laboratories, Inc.) or unconjugated Fab Fragment (115-007-003 Jackson ImmunoResearch Laboratories, Inc.) for 2 h then vigorously rinsed 8 times with 1× PBS for 4 min/rinse.

Following blocking, sections were incubated in a primary antibody solution consisting of 5% goat serum, 0.1% triton X-100, and antibodies against neuronal nuclei (1:250 NeuN MAB377 Millipore), microglia (1:500 Iba-1 NC9288364 Fisher), and/or tomato-plant lectin (1:200 B-1175 Vector Labs) for 18 h at 4 °C. Sections were then washed with PBS (3 × 5 min) and incubated in a secondary solution consisting of 5% goat serum, 0.1% triton X-100, and antibodies (1:500 goat anti-mouse Alexa 488, Invitrogen; goat anti-rabbit Alexa 568, Invitrogen; and/or Dylight 649 Streptavidin, Vector Labs) for 2 h at room temperature. Sections were then rinsed with PBS (3 × 5 min), exposed to 1:1000 Hoechst 33342 (Invitrogen) for 10 min, and washed in PBS (3 × 5 min) before being coverslipped with Fluoromount-G (Southern Biotech, Birmingham AL). Sections were promptly imaged using confocal microscopy (FluoView 1000, Olympus, Inc., Tokyo, Japan) at 20× magnification over V1.

3. Results

Single shank 16 channel linear silicon electrode arrays with 100 micron site spacing were chronically implanted into the left monocular visual cortex of eight mice. During each recording session, the animals were shown whole field drifting gratings on a computer screen under very light gas anesthesia. For single-unit analysis, impedance, and noise floor, the animal number is $N = 8$ day 0 to day 8, $N = 7$ day 14 to day 35, $N = 6$ day 42–133, and $N = 4$ day 140 to day 189 (Table 2). (One animal was removed due to health complications unrelated to the surgery/implant, the next was removed for early histology, the last two were removed early following months of complete loss of SUA or MUA and very high impedances). For evoked MU analysis, the two early time point animals (7 day and 35 day) which were included for SUA analysis were excluded from MUA analysis due to issues with system delays in Psychtoolbox; $N = 6$ days 0–133, and $N = 4$ days 140–189.

3.1. Stimulus presentation improves electrophysiological characterization

Automated spike sorting showed that an increased number of units could be detected under visual stimulation as compared to the spontaneous condition. Fig. 2a shows an example electrode recording under resting state conditions (i.e., with the monitor turned off). Here, the algorithm was unable to detect any SUs and shows the firing rate of only the unsorted outlier threshold-crossings after PCA (Fig. 2a; black). However, in the presence of an 8-direction, 4 s 'ON', 4 s 'OFF' stimulation, a slow firing, high amplitude unit was detected on the same recording site during the stimulus (Fig. 2b and e; green). When the screen was occluded with cardboard, the visual

Table 2
Animals.

Animal #	Days	SU	Impedance	MU	LFP	Reason for removal
1	7	X	X			Non-surgical Health Complications
2	35	X	X			Early Histology
3	133	X	X	X	X	Histology: No Signal & High Impedance
4	133	X	X	X	X	Histology: No Signal & High Impedance
5	189	X	X	X	X	End of Study
6	189	X	X	X	X	End of Study
7	189	X	X	X	X	End of Study
8	203	X	X	X	X	End of Study

stimulation did not induce any evoked response. The firing rate of the green unit in Fig. 1b shows that the rate increases the most during the visual stimulation. In addition, LFPs recorded at the same time show substantial stimulus dependent activity (Fig. 2c). At the same electrode, a 2 s long spike stream during one of the 8 repeats of 8-direction, 1 s 'ON', 1 s 'OFF' stimuli shows increased number of high amplitude spikes during the 'ON' stimulus (Fig. 2i). Automated spike sorting detects a second high firing, but low amplitude unit in addition to the green unit that was present during the slower stimulation (Fig. 2f–h, blue). PSTH show that both SU increase firing rate during the 'ON' stimulus. Some SU demonstrated strong tuning curves, but others did not. However, it has been well characterized that in primary visual cortex, many neurons do not exhibit strong tuning preferences, such as luminance, adaptation, position, and contrast cells (Antolik and Bednar, 2011; Dai and Wang, 2012; Gavornik and Bear, 2014; Harding and Fylan, 1999; Jeyabalaratnam et al., 2013; Niell and Stryker, 2008; Vetter et al., 2014). Therefore, this work focuses on longitudinal characterization of broad evoked firing rate changes. Furthermore, without a tetrode configuration or intracellular electrodes, a single recording site cannot discriminate between two SU with similar waveforms but distinct tuning curves, which is further complicated by the salt-and-pepper organization of the rodent cortex (Jeyabalaratnam et al., 2013). In addition, previous studies have demonstrated that the awake cortex is dominated by inhibition (Haider et al., 2013). Our study confirms these findings (Fig. 3ab). These results suggest that for the purposes of identifying electrode sites capable of detecting MU activity, proper anesthesia levels can allow for greater evoked SNFRR. In addition, proper anesthesia levels dramatically reduce movement induced electromagnetic noise, which cannot be completely isolated from MU.

3.2. Characterizing the evoked response

The LFP spectrogram for this channel shows increased ~70 Hz gamma oscillations during the 'ON' stimulus, and a brief increase around 45 Hz and its second harmonic 90 Hz immediately following the end of the stimulus (Fig. 2c). Power spectrum analysis confirmed the observations in the LFP spectrogram (Fig. 2j). Strong power can be observed around 70 Hz during the 'ON' stimulus and 45 Hz during the 'OFF' stimulus. Interestingly, the 'OFF' LFP response only lasts about 1 s. Because activation is very brief and weak, it becomes averaged out when the LFP power is averaged across the entire 4 second 'OFF' period following the stimulus. However, during the 1 s stimuli, greater response can be observed at 45 Hz and 90 Hz during the 'OFF' stimulus and a slight shifting of the ~70 Hz 'ON' peak toward 60 Hz and 75 Hz (Fig. 2k). Therefore, 1 s stimuli were used for evoked neural activity around the implanted array. When the screen was covered with a cardboard box, the visual stimulation did not evoke the 'ON' or 'OFF' gamma response.

3.2.1. Optimization of evoked MU activity

Significant evoked response yield for each array was characterized through a paired *t*-test of the number of threshold crossings in equal sized bins immediately before and immediately after the stimulus for each electrode site (Fig. 3c and d). Because there are synaptic delays between the light hitting the retina and the signal reaching the visual cortex (Bair et al., 2002; Marshall et al., 1943; Niell and Stryker, 2008; Raiguel et al., 1989; Schmolesky et al., 1998; Vogels and Orban, 1994), *t*-tests were also calculated at −50 ms, 50 ms, 100 ms, and 150 ms offsets from the stimulus onset to account for synaptic delays. As expected, a negative delay showed the least yield. Negative delay may still demonstrate a significant MU yield if the width of the bin size is large enough to be dominated by their appropriate 'ON' or 'OFF' state (Fig. 3d).

The first task of characterizing the visually evoked response was to identify how to best quantify visually evoked neural activity longitudinally. For this, a simple paired *t*-test was applied between the number of neural threshold crossing in equal sized time bins before and after the stimulus (Fig. 3d). The results suggest that increasing the bin size can increase the ability of the *t*-test to identify significant changes in firing rate. This may partly be because there is more data to compare differences and reduce error as well as reduce inhibition from anesthesia (Haider et al., 2013). There are also different types of neurons in the cortex that have different roles, and therefore have different temporal dynamics (Gao et al., 2010; Lennie, 1981; Raiguel et al., 1989). For example neurons responding to luminance changes likely activate more quickly than neurons involved in the inhibition response. Another important note for this *t*-test is that 8 repeats of 8 directions "1s 'ON'"-"1s 'OFF'" were used to maximize evoked activity as described in the previous section. The 'OFF' duration is not identical to spontaneous "resting state" condition and has its own firing pattern and LFP profile, which can be seen in Fig. 2a–c as well as Fig. 2j–k. It is likely that a combination of these factors lead to the observation of peak yield responses in bin sizes of both 550 ms and 850 ms. Anesthesia may also play a role in this, as it has been shown to make evoked responses broader and longer than under awake conditions (Haider et al., 2013).

In addition to varying bin size, different durations of delay have also been compared. It is well known that there is a delay between when the light hits the retina and when the signal reaches the cortex (Bair et al., 2002; Marshall et al., 1943; Raiguel et al., 1989; Schmolesky et al., 1998; Vogels and Orban, 1994). Fig. 3d shows that the peak yield occurs when a 50 ms delay and a bin size of 550 ms is used for the *t*-test. This ~50 ms delay is also observed in CSDs of both the 'ON' and the 'OFF' response (Fig. 2a and b) and is consistent with latencies characterized in the literature (Bair et al., 2002; Marshall et al., 1943; Niell and Stryker, 2008; Raiguel et al., 1989; Schmolesky et al., 1998; Vogels and Orban, 1994). As expected, the *t*-test performs the worst when a −50 ms delay is used, since 100 ms of the "OFF" response replaces the 'ON' response data in the test. Ultimately, 550 ms bin with a +50 ms delay showed the greatest yield and statistical significance against all other data points except for 600 ms bin with a +50 ms delay ($p < 0.05$). Therefore, 550 ms bin with a +50 ms delay was used to quantify the detection of significant evoked MU activity for the remainder of the study.

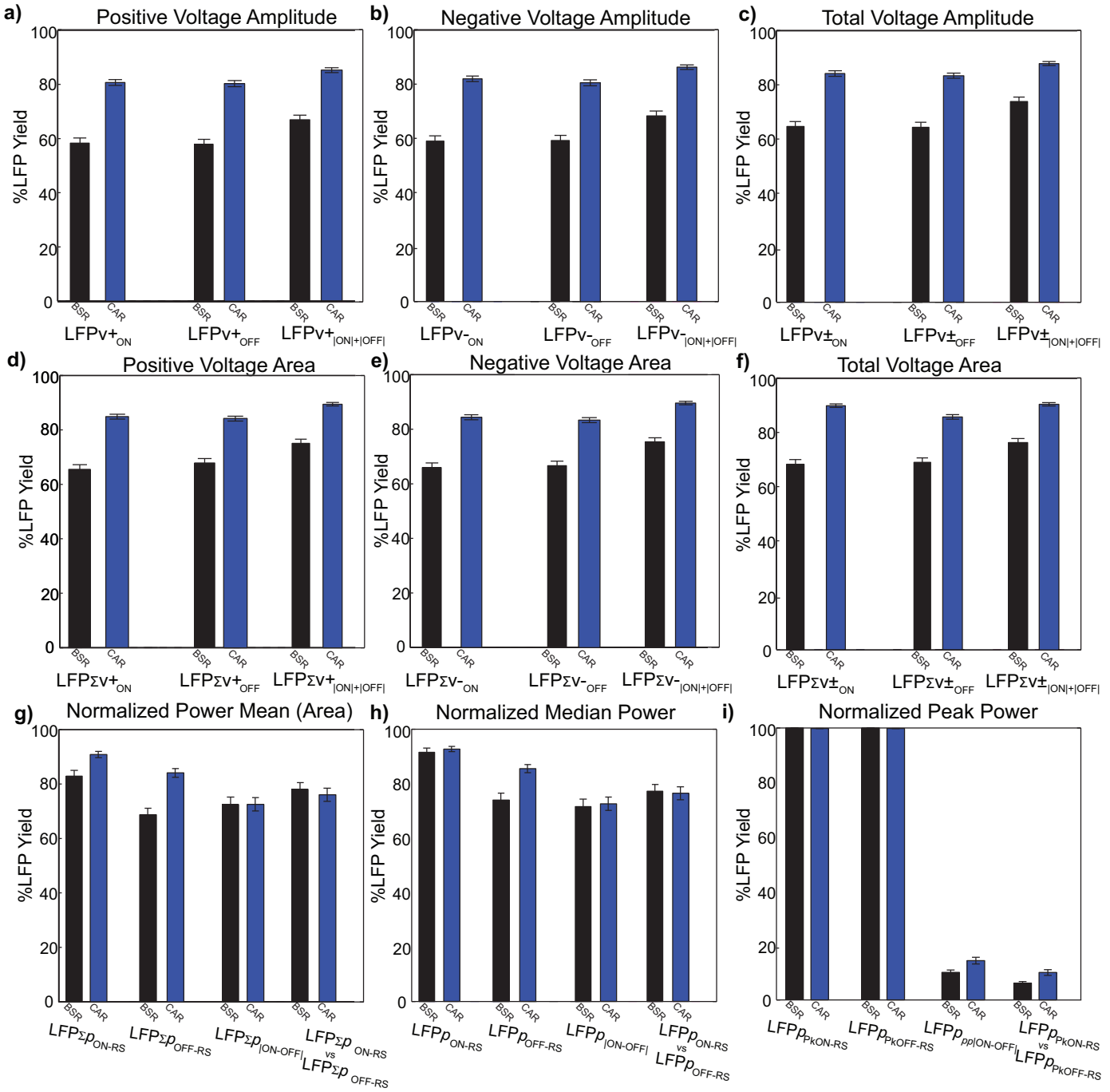

Fig. 5. Optimization of LFP yield using contralateral bone screw ECoG reference (black), and CAR (blue). (a)–(c) Total yield using positive (a: Eq. (4)), negative (b: Eq. (5)), and total (c: Eq. (6)) amplitude of the LFP *voltage* response for ON, OFF, and the peak-to-peak magnitude of ON–OFF. (d)–(f) Total yield using positive (d: Eq. (7)), negative (e: Eq. (8)), and total (f: Eq. (9)) area of LFP *voltage* response for ON, OFF, and the peak-to-peak magnitude of ON–OFF. (g) and (h) Total yield using subtraction normalized LFP *power* response (dB) mean (g) and median (h) (Eqs. (10) and (12)), and peak (i: Eqs. (14)–(15)),. (g) Mean of LFP power response for ON, OFF, |ON-OFF| and ON vs. OFF. (h) Median of LFP power response ON, OFF, |ON-OFF| and ON vs. OFF. (i) Yield is shown for the peak-to-peak LFP power for ON, OFF, | ON-OFF|, and ON vs. OFF. (For interpretation of the references to color in this figure legend, the reader is referred to the web version of this article.)

3.2.2. Optimization of evoked LFP activity

LFP voltage amplitude, voltage area, and power have been previously used to quantify LFP activity (Jia et al., 2011; Land et al., 2013b; Xing et al., 2012) (Table 1, Figs. S1 and S4). Similar to evoked MU, evoked LFP yield was defined as the number of recording sites able to detect significant evoked LFP activity. Therefore, significant evoked response yield for each array was characterized through a paired *t*-test against pseudo triggered resting state activity using each of these metrics (Eqs. (4)–(15)). For LFP characterization, the yield from different normalization metrics and characteristics of the responses were compared using LFP power and voltage (Fig. 5, Fig. S5). Although electrodes were implanted into monocular visual cortex to reduce neuronal input from the contralateral eye, it is still possible that the ECoG signal detected in the contralateral bone screw reference may influence the LFP signal. Therefore, CAR was employed to examine ECoG influence on the LFPs. Applying CAR to LFP voltage and LFP power improved yield relative to bone screw reference LFP voltage for

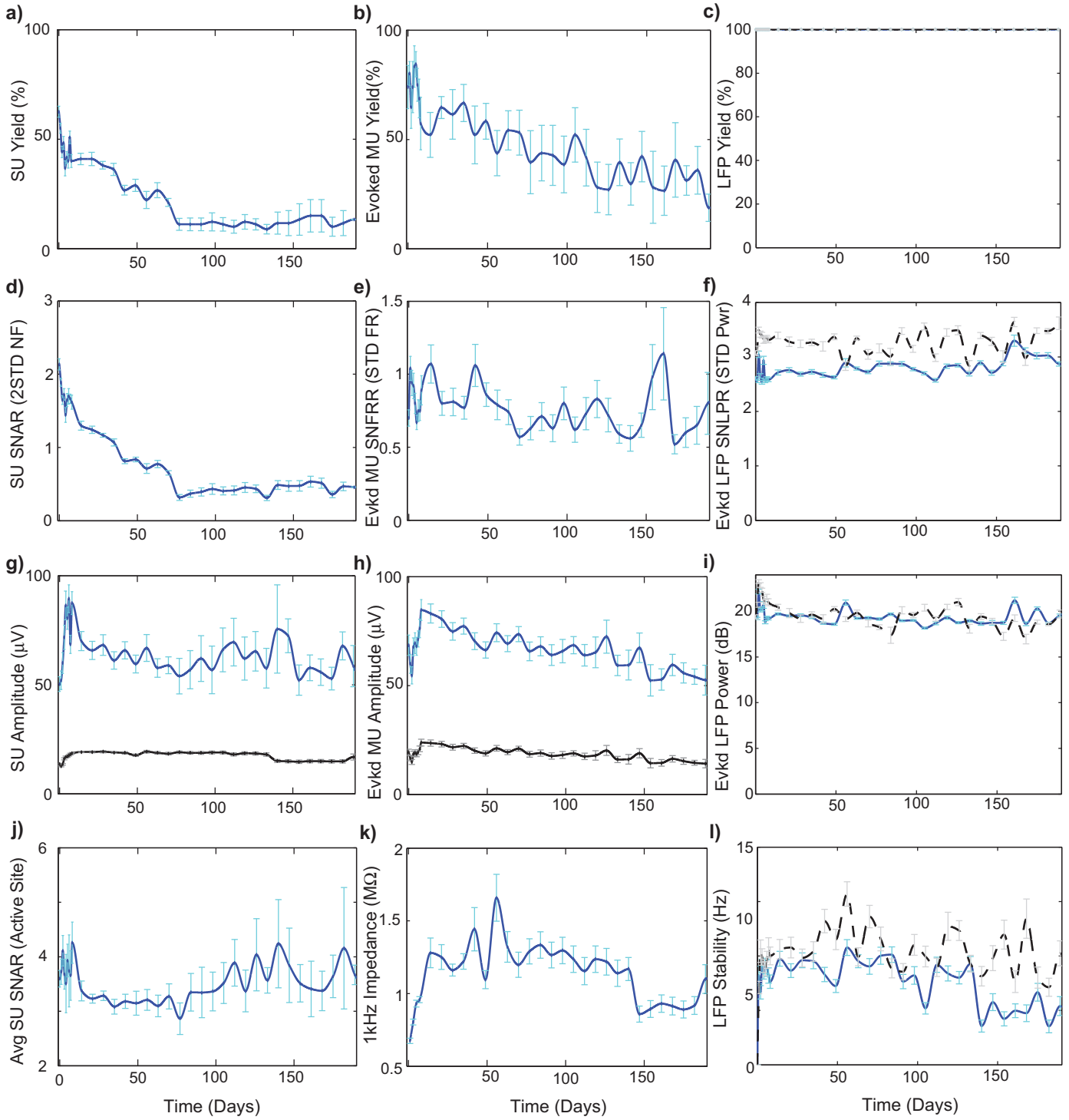

Fig. 6. Chronic electrode performance. (a)–(c) Signal yield of SU (a), significant evoked MU (b), and significant evoked LFP (c) over days (blue: contralateral bone screw reference & black dashed: common average reference). (d)–(f) Signal quality of SU (d) SNAR, MU (e) SNFRR, and LFP (f) SNLPR over days. (g)–(i) Signal strength of SU (g: amplitude), MU (h: amplitude), LFP (i: power). (j)–(l) Signal Steadiness of SU SNAR of only active recording sites (j), 1 kHz impedance (k), and frequency shifts in the peak LFP power (l) over time. (For interpretation of the references to color in this figure legend, the reader is referred to the web version of this article.)

ON vs. RS and OFF vs. RS (Fig. 5). The removal of the common signal, whether the signal was influenced by contralateral bone screw ECoG signal or common signal along the cortex, reduced the baseline power, uncovered buried LFP features (Fig. S3), and increased the LFP power spectrum difference between the evoked and resting state activity. Interestingly, there were little differences in yield among the LFP voltage quantification methods tested (Fig. 5a–f, Fig. S1).

For LFP power, the power decreased with increasing frequency without normalization (Fig. 4a and b). Normalizing the visually evoked LFP power spectrum by subtracting the resting state power spectrum using Eq. (10) highlighted key LFP features that were activated during visual stimulation (Fig. 4c and d). The normalization by the dividing resting state spectrum more heavily weighs higher frequency activity due to the decreasing resting state power in higher frequency bands (Fig. 4, Fig. S5). In visual cortex across

the frequencies examined, evoked activity generally led to large power increases in the lower frequency bands. Therefore, subtraction normalization instead of division normalization resulted in significantly greater yield ($p < 0.05$) or equal yield (100%) for all comparisons in this particular study.

While there appear to be common frequency bands associated with the 'ON' and 'OFF' response, the exact frequency can depend on the animal (Fig. S2). Interestingly, the LFP power peak frequencies for 'ON' and 'OFF' are largely conserved along the depth and across time in mice (Fig. 4e–h, Fig. S3). While multiple evoked LFP voltage and power quantification methods were evaluated, the peak-to-peak quantification of the normalized power spectra produced the greatest significant yield and the most sensitive metric. This may because the peak-to-peak metric is independent of the exact frequency of the evoked gamma band which can differ between animals and electrode placement. In addition, peak-to-zero (MAX or MIN) normalized frequency power led to lower evoked LFP yield, possibly due to the variability in noise across trials.

Furthermore, because OFF is a visually evoked response with high power gamma-band activity, normalizing ON by OFF instead of resting state activity may subtract significant evoked power activity and artificially reduce the evoked power toward resting state baseline levels, and at the same time $|RSp_{pseudoON} - RSp_{pseudoOFF}|$ may result in increasing the noise during the statistical test. Because the ON yield was significantly greater ($p < 0.05$) than OFF yield for both median and mean analyses method and ON is a longer sustained response compared to OFF (Fig. 2c), ON was utilized to characterize LFP for the remainder of the study.

3.3. Depth independent chronic electrode performance analysis

3.3.1. Signal yield

In this section, performance metrics were averaged across all 16 electrodes along the shank without consideration of recording site depth. First, the percentage of recording sites able to detect SU signal was quantified as yield. Depth independent SU yield (percentage of electrode sites able to detect a SU) (Fig. 6a) and the yield of recording sites able to detect significant evoked MU activity response (SU and MU) (Fig. 6b) showed that more channels were able to detect MU activity than SU waveforms. Similarly, yield of recordings sites able to detect significant evoked LFP activity (Fig. 6c) was greater than channels able to detect MU activity or SU waveforms (additional details in Supplementary Information S4.3).

3.3.2. Signal quality

The quality of the detected SU signal was quantified as SNAR (channels with no detectable SUs were considered to have SNAR = 0). Average SU SNAR declined over time until day 77 where it stabilized (Fig. 6d). The evoked SNFRR and SNLPR was only evaluated for channels showing significant evoked activity. Evoked MU SNFRR and LFP SNLPR showed a more limited decline than SU SNAR (Fig. 6d–f).

3.3.3. Signal strength

Signal strength of the detected signal was quantified as signal amplitude. The average amplitude of the recorded SUs peaked between day 6 and 8 then quickly declined to day 14, and then more slowly declined to day 70 (Fig. 6g). On the other hand, noise floor increased over the first 14 days then generally remained stable. The largest reliable MU amplitudes of activity dependent channels were estimated by calculating the mean amplitude plus two standard deviations of isolated units that were on channels detecting significant evoked activity. The evoked MU amplitude of all units (SU + MU) peaked in the 2nd week, and then declined slowly and steadily (Fig. 6h). The Vrms amplitude of evoked units followed the same trend to MU amplitude over time. In general, the evoked MU

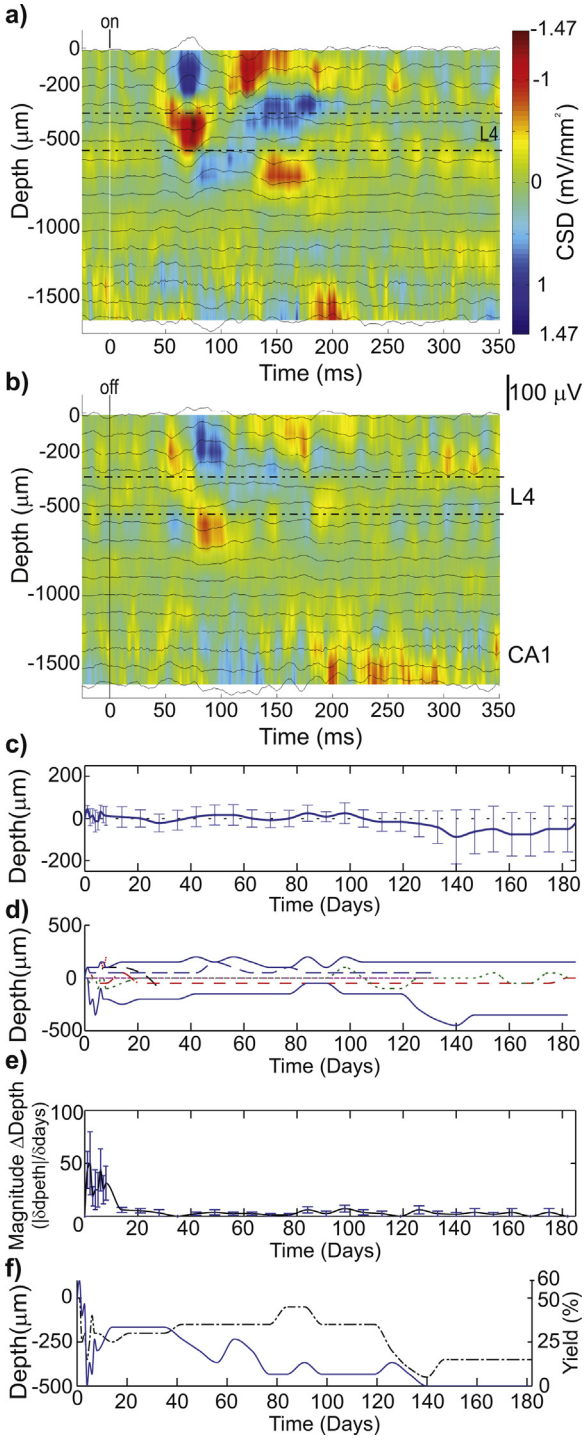

Fig. 7. Layer IV of the visual cortex. (a) CSD following the 'ON' stimulus. (sink = red; source = blue). Layer IV is indicated by a strong electrical sink followed by a strong source. *Note*: ~50 ms delay. (b) CSD following the stimulus turning off. *Note*: Mild activation of layer II/III followed by layer V and ~50 ms delay. (c) Average depth position of layer IV compared to day 0. (d) Depth position of layer IV of each animal over days. (e) Magnitude of average depth change shows that layer IV fluctuates greatly during the first two weeks, but stabilizes thereafter. (f) In one animal, position of layer IV (dashed line) drastically sank deeper along the electrode. It sank greatly during the first week, then recovered, then sank again 4–5 months later. Recording yield (solid line) followed a similar trend. (For interpretation of the references to color in this figure legend, the reader is referred to the web version of this article.)

amplitude showed a more stable decline than SU amplitude. Evoked LFP signal strength was quantified as the peak of the LFP power after normalization to resting state baseline. LFP power declines slightly during the first week, but remains more stable then the SU or MU signal strength (Fig. 6i).

3.3.4. Signal steadiness

Interestingly, even though the SU yield and SNAR both declined until day 77, the SU amplitude of recorded units did not drastically change in a similar trend. Examining the SU SNAR of only electrode sites actively recording a SU shows that the average SU fluctuated over the first 8 days, but stabilized between days 14 and 77 (Fig. 6j). It then slowly increased. This discrepancy may provide insight into the tissue stabilization discussed further below.

Impedance increased from $675 \pm 116\,k\Omega$ to $1280 \pm 237\,k\Omega$ over the first 14 days (Fig. 6k). It fluctuated around this value for the next several weeks, but stabilized on day 70. Note that the sharp decline at day 140 is due to the removal (sacrifice) of the highest impedance animals that were no longer recording any SUs. This further demonstrates the variability of impedances. However, significantly sharp changes were not detected across metrics other than noise floor and impedance, suggesting limited correlation.

LFP stability was quantified as the drift of the peak evoked LFP power over time. The peak frequency of evoked LFP power is generally very stable over time (Fig. 6l) and along different depths in mice, though it can vary across the cortex.

3.4. Electrophysiological identification of layer IV

Using visually evoked stimulation paradigm with a linear array has an added benefit of enabling the identification of cortical layers longitudinally without an imaging window or chronically implanted prism which will induce its own tissue response. It is well understood that layer IV is the primary recipient of thalamocortical projections. Because of this, layer IV can be identified using current source density analysis (Jin et al., 2011; Mitzdorf and Singer, 1978; Smith et al., 2013; Stoelzel et al., 2009). Following the onset of the 'ON' stimulus a strong electric sink is observed in layer IV prior to a strong electric source. This is generally followed by a strong sink in layer II/III and layer V (Harris et al., 2010).

Current source density (CSD) was used to identify a strong electrical current sink of layer IV in the visual cortex (Fig. 7a, see Supplementary Information for additional details) shortly followed by a sink in layer II/III, and then layer V. After the stimulation turns 'OFF,' weaker sinks can be observed in layer II/III and layer V (Fig. 7b). The 'OFF' response usually shows sinks in layer II/III then V followed by sinks in the very shallow layers and then the CA1 region around the Stratum Pyramidale. This again discriminates the distinct 'OFF' response from the 'ON' response. This 'OFF' response may provide insight on how adaptation is released (Bair et al., 2002; Jin et al., 2011; McGuire et al., 1984). Note, both 'ON' and 'OFF' CSDs have a ~50 ms delay before the first current sink.

The depth of layer IV on the day of the surgery is defined as 0 μm in Fig. 3c–f. Examining the changes in the depth of layer IV over time shows that while there are some fluctuations in depth during the first week, it stabilizes by 14 days (Fig. 7c–e). Therefore, the average depth of layer 4 between day 14 and day 120 was used for depth related analysis. Lastly, examining the individual SU yield of the animal with the dramatic layer IV depth change shows that the drop and recovery of SU yield trends very closely with the drop and recovery of layer IV depth (Fig. 7f). After sacrificing this animal, it was noted that the brain had substantially less volume compared to the other animals, though no signs of infection were detected. (See Supplementary information S4.4)

3.5. Depth dependent chronic electrode performance analysis

Probe implant depths were aligned across animals at their average layer IV depth between day 14 and day 100 (Fig. 7). Layer IV was determined with CSD following the visual stimulus.

3.5.1. Signal yield

Of immediate note is that cortical layers play a critical role in chronic SU yield (Fig. 8a, Table S1). For example, Layers IV to VI have the greatest yield acutely, but Layers II to IV have the best cortical yield in chronic time points. In contrast, visually evoked MU (including SU) yield was much greater across all depths. However, depth dependent features can still be observed (Fig. 8b, Tables S2 and S3, Fig. S6b). While SUs were not detected in the most superficial layer, visually evoked MU activity was detected $\sim 30 \pm 26\%$ throughout the experimental period. Yield did not appear to have strong depth-dependence with LFP as noted with SU and MU (Fig. 8c, Fig. S6c). However, at very chronic time points, yield appeared to fluctuate in deeper layers. This may be due to the increased probability of mechanical failure of planar electrode arrays in deeper layers (Kozai et al., 2015a).

3.5.2. Signal quality

Signal quality and signal quality change over time was also dependent on recording layer. The SU SNAR follows the same trend as the SU yield (Fig. 9a, Table S4). To better display the average SNAR of the detected units across depth (Fig. 5a), channels that did not detect SUs were considered to have an SNAR equal to the noise floor (2 standard deviations). To quantify functional MU activity, a new evoked SNFRR metric was developed. Here, the change in firing rate between 'ON' and 'OFF' was measured as "signal" while the average standard deviation of all the 'ON' and 'OFF' firing rate was calculated as "noise" (Fig. 9b, Tables S5–S6, Fig. S7b). To better display the average evoked SNFRR, firing rates were only averaged if significant activity was detected. A value of zero signifies that no significant activity was detected on a certain day at that certain depth. LFP signal quality was quantified using SNLPR of the evoked power ON response. In contrast to the SU SNAR and MU SNFRR, the SNLPR remained stable, especially between Layer I and CA1 stratum pyramidale layer (Fig. 9c, Fig. S7c).

3.5.3. Signal strength

Signal strength and signal strength change over time showed dependence on recording depth. The average SU amplitude (Fig. 10a, Table S7) followed a similar trend to the SU yield. MU amplitudes on channels detecting significant evoked activity showed slower amplitude decreases over time compared to SU amplitude (Fig. 10b, Tables S8–S9, Fig. S8b). Together these data show that rate of charge across electrophysiological performance metrics are dependent on the layer they record from. The peak power of significant evoked LFP (normalized by resting state LFP power: Eq. (10)) followed a similar pattern to SNLPR, suggesting minimal influence from noise (Fig. 10c, Fig. S8c), at least with the experimental setup used in this study.

3.5.4. Electrochemical stability

Similarly, longitudinal impedance changes occur over time in a depth dependent manner (Fig. 11a, Table S10). Impedance generally increased over the first week, but at different times in different layers; the impedance appeared to increase first from the tip of the electrode as well as from the surface, leaving Layer II/III to experience the increase in impedance last. It also becomes apparent that the impedance drastically changes in the cortex and subcortical white matter region over the first 77 days, both increasing and decreasing. On the other hand, impedance in the CA1 shows a dramatic increase in impedance over the first week, but decrease

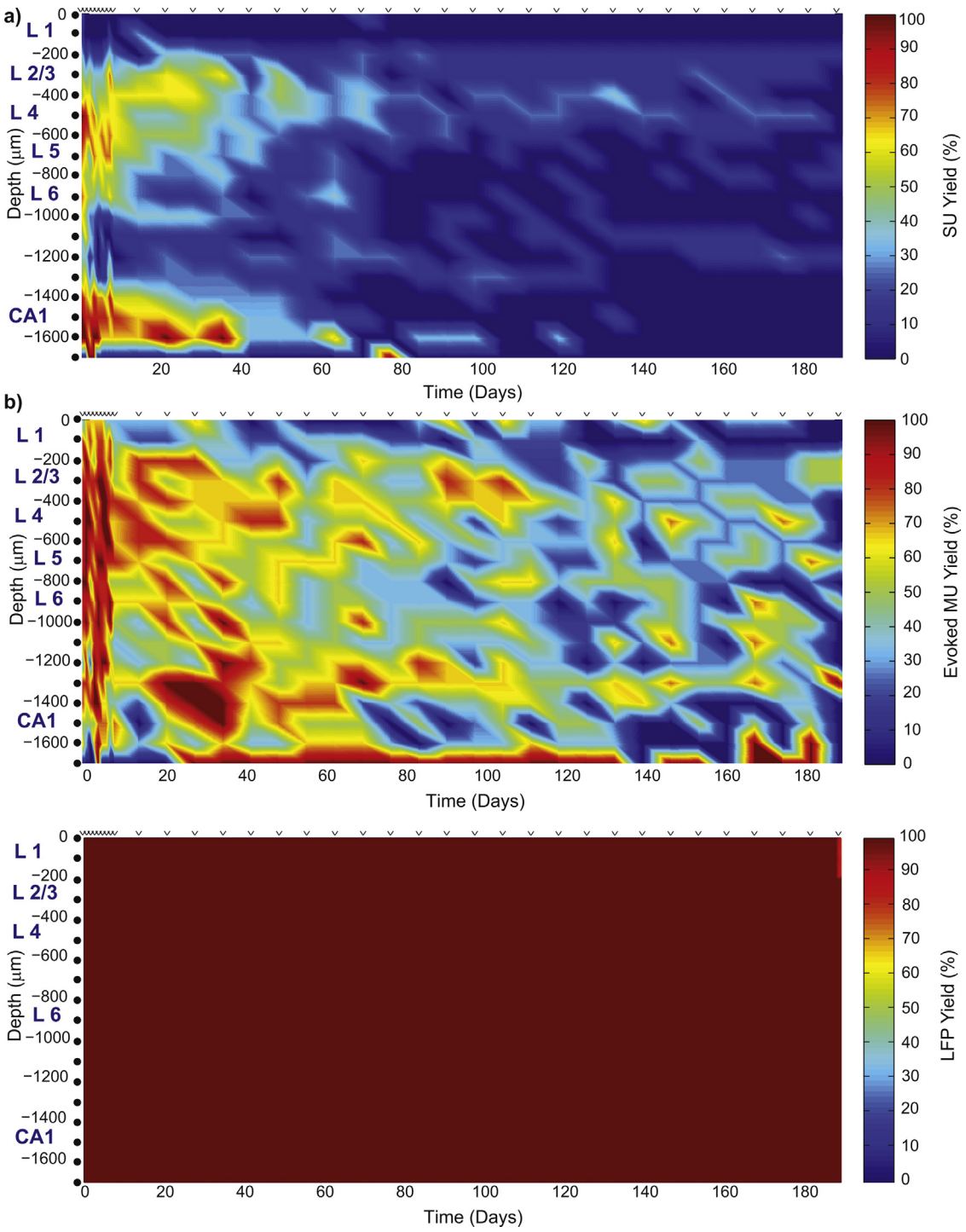

Fig. 8. Recording yield as a function of depth and time. (a) SU. (b) Activity dependent unsorted units. *Note*: there are greater yields around layer IV and in CA1. (c) LFP. Strong yield calculated across depth and time using evoked ON response.

again over the next 21 days. While subtle changes occur within a layer after day 77, these changes are much more muted than during the first 77 days. Noise also showed initial increase to be greatest in layer I and the deepest recording site (Fig. 11b, Fig. S9b, S10). For LFP, the frequency bands of the evoked LFP power remain similar across depth, and through time. Therefore, LFP stability was measured as the shift in the peak frequency relative to the peak frequency on the first day a significant evoked response was detected (Fig. 11c, Fig. S9c). In general, shifts in the peak LFP frequency were very limited. Large shifts were mostly detected in the deepest recording sites, and associated with large drops in impedances. Material failure of the insulation with planar silicon electrodes in these deep recording sites may alter the bulk capacitive property of the electrode and artificially shift or filter the recorded raw LFP data stream from the actual LFP signal (Kozai et al., 2015a).

3.6. Electrochemical stability for neural spike and LFP recordings

1 kHz impedance is a good metric for monitoring the electrochemical electrode properties for recording the 1 ms waveforms of neural spikes. However less is known about impedances at the LFP

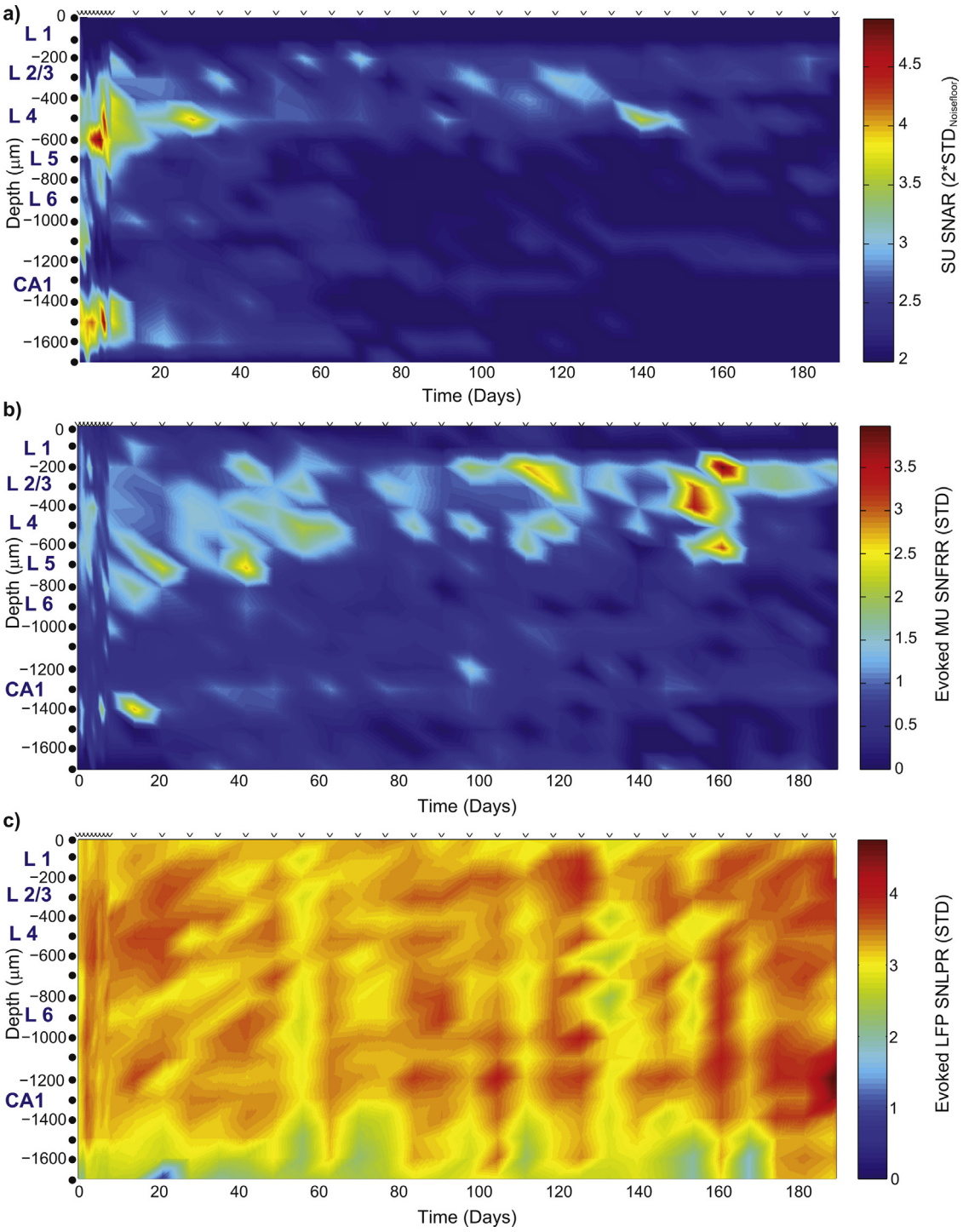

Fig. 9. Signal quality: SNR as a function of depth and time. (a) SU SNAR (voltage). (b) Evoked SNFRR of activity dependent unsorted MUs. *Note*: greater SNR is detected around layer IV and in CA1. (c) LFP SNLPR using power of normalized ON response with CAR. Increase in SNLPR seen between days 100 and 140, and overall low SNLPR throughout the experiment. Zeroes were separated in the heat maps to better illustrate the signal quality across layers. Probability of recording a significant signal can be examined via the yield plots.

range (10–100 Hz) and how they correlate to LFP recording performance. Fig. 12 shows the depth independent impedances for 10 Hz, 42 Hz, 57 Hz, and 100 Hz. The 42 Hz impedance was reported because it was the frequency of the peak power density spectra of the average 'OFF' response (Fig. 4c and d). Similarly, 57 Hz impedance was reported because it was the frequency of the peak power density spectra of the average 'ON' response (Fig. 4c and d). Naturally, the impedance magnitude is larger with lower frequencies. While subtle differences can be observed across different frequencies, the overall pattern of impedance fluctuation over time is fairly similar. The depth dependent LFP range impedances are shown in the heat maps (Fig. 13). Lower frequency impedance show slightly different peaks and patterns compared to 1 kHz impedance heat map, but the overall pattern is similar across frequencies

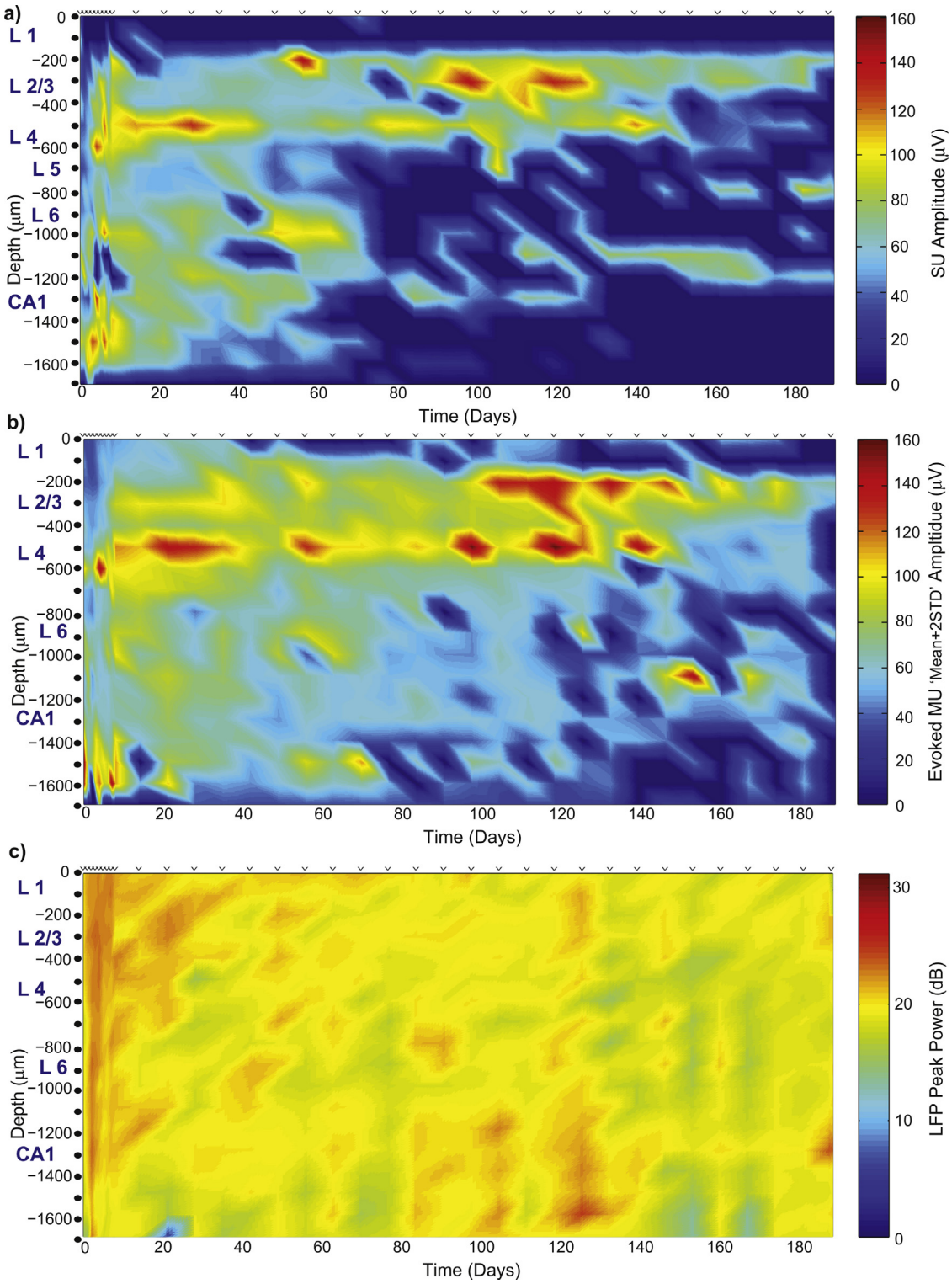

Fig. 10. Signal strength as a function of depth and time. (a) Mean SU voltage amplitude. (b) Mean voltage amplitude + 2*STD of activity dependent unsorted units. *Note*: greater amplitude is detected around layer IV and in CA1. (c) LFP peak power of the ON response. *Note*: increase in peak power occurs at same depth and days as SNLPR increase is seen in Fig. 8c. Zeroes were separated in the heat maps to better illustrate the signal quality across layers. Probability of recording a significant signal can be examined via the yield plots.

4. Discussion

4.1. Visually evoked stimulation can increase sortable SUs and enable MU/LFP characterization

As expected, evoked stimulation can increase the firing rate of low firing or quiescent neurons (Shoham et al., 2006), and can improve spike sorting yields from automated cluster algorithms (Fig. 2a–i). SUs that are identified only during evoked stimulation are not necessarily low amplitude units, but rather can be high amplitude units that are only activated when specific input conditions are met. This confirms the idea that neurons immediately adjacent to the electrode recording site may not be detected under spontaneous "resting state" conditions (Henze et al., 2000). In turn,

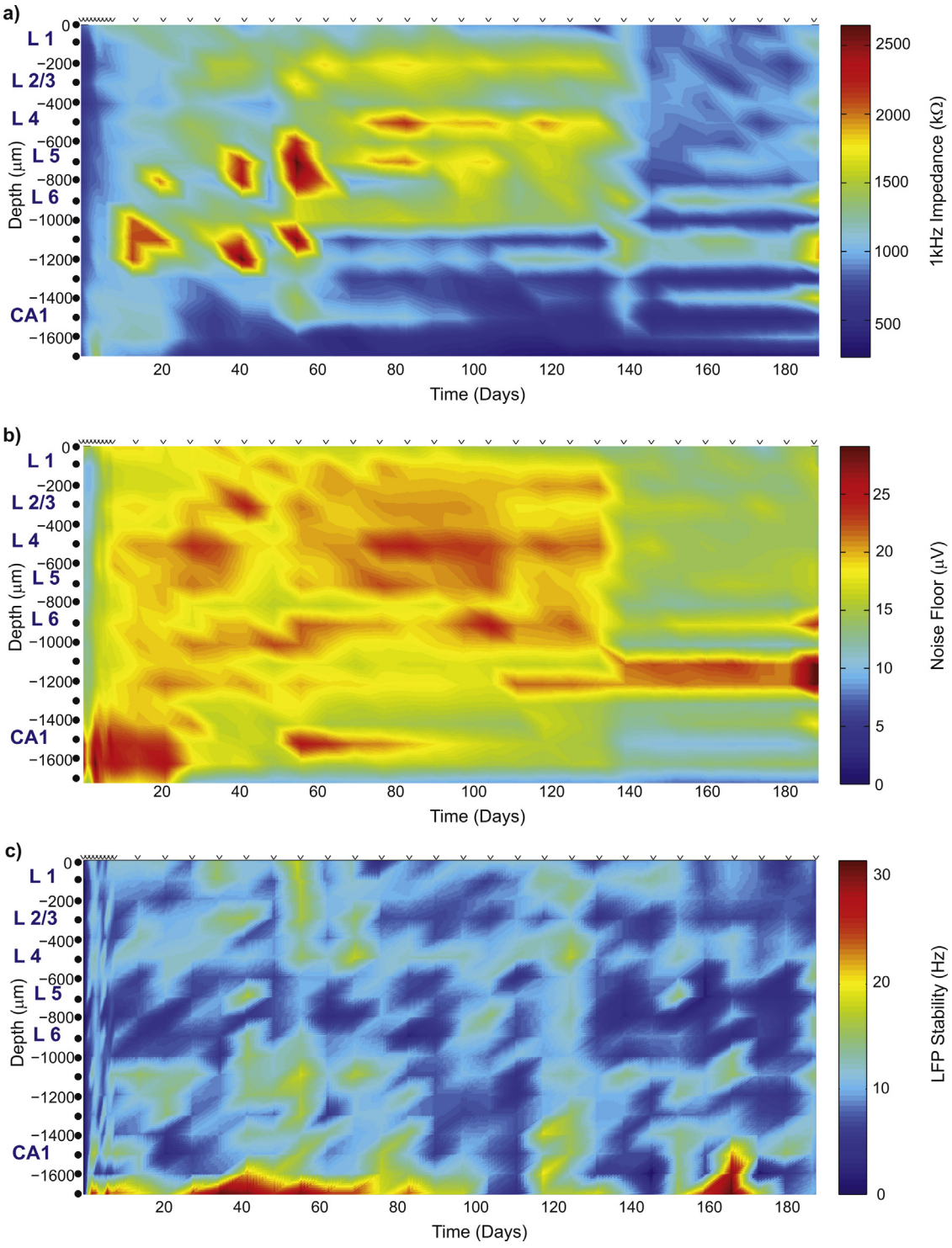

Fig. 11. Electrochemical stability (a) 1 kHz impedance. (b) Noise floor voltage. *Note*: early increases in impedance in the region bordering hippocampus and cortex as well as increases in impedance of the deeper layers. Also note: high impedance in region bordering hippocampus and cortex of later time points. (c) LFP stability measured as frequency shift of peak ON power.

this implies that an electrode that is unable to detect a SU does not necessarily mean the site has failed, or that it has become unusable due to the reactive tissue response. Therefore our current strategies of recording sensory evoked neural activities provide an improvement in accuracy of detecting functional electrodes.

A major advantage of visually evoked stimuli is the ability to quantify evoked MU and LFP activity. For the purposes of characterizing a recording site's ability to detect significant MU and LFP, it was desired to evoke responses from as many neurons as possible. We chose to use full-field gratings with different orientations separated by black 'OFF' screens. Gratings are an effective stimulus for neurons in visual cortex, and the black screen 'OFF' state also activates neurons that detect luminance change during the transition from 'ON' to 'OFF' as well as 'OFF' to 'ON' (Murray et al., 2002). While a fixed grating size, temporal drift frequency and grating spacing were employed in this study, adjusting these parameters

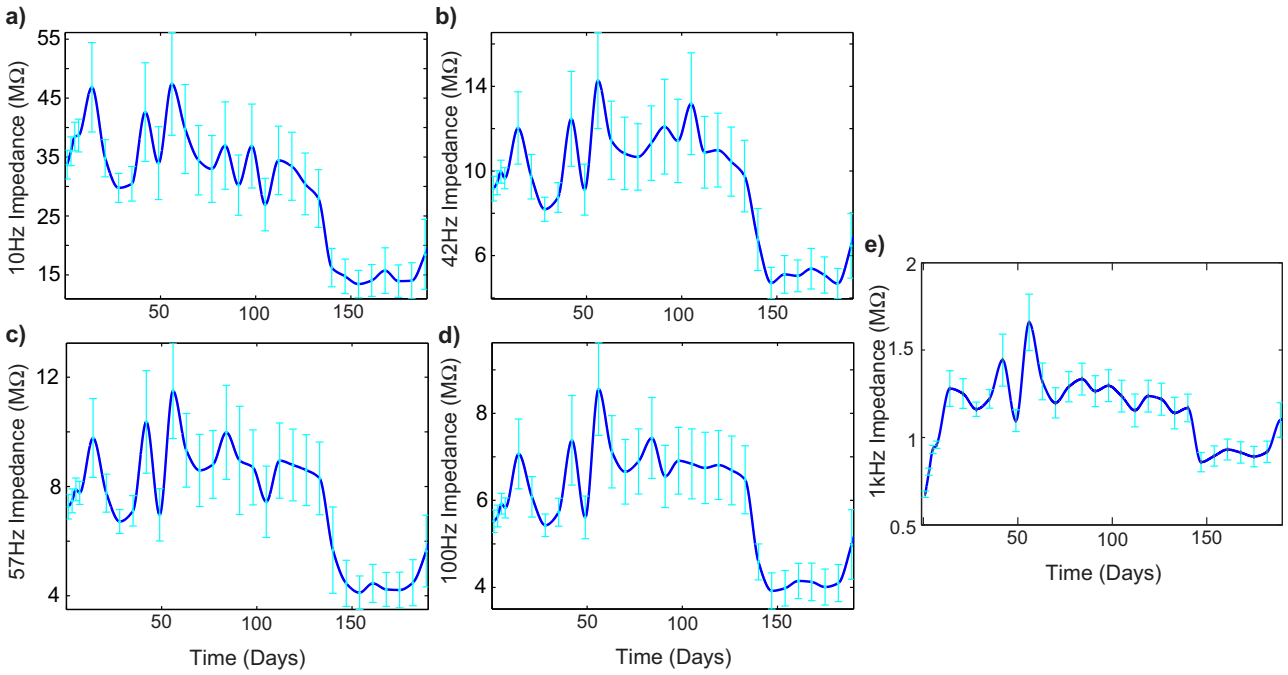

Fig. 12. Impedance from LFP range. (a) 10 Hz impedance. (b) 42 Hz impedance (frequency of peak average power of 'OFF' response). (c) 57 Hz impedance (frequency of peak average power of 'ON' response). (d) 100 Hz impedance. (e) 1 kHz impedance.

could evoke responses in additional neurons that were unresponsive to our stimulus due to their spatial and temporal frequency tuning, or to surround suppression to the large grating. Nonetheless, most neurons in visual cortex are sensitive to stimuli with a broad range of spatial and temporal frequencies and sizes (De Valois et al., 1982; Jeyabalaratnam et al., 2013; Land et al., 2013b), so we expect that our choice of stimulus type did not greatly impact the size of the evoked population. It has also been well characterized that not all units in the visual cortex exhibit strong tuning curves due to lateral inhibition or because they preferentially encode luminance, adaptation, or contrast changes (Antolik and Bednar, 2011; Brodie et al., 1978; Dai and Wang, 2012; Foster et al., 1985; Harding and Fylan, 1999; Jeyabalaratnam et al., 2013; Kuhlman et al., 2011; Olsen et al., 2012). Therefore, the focus of this study was to characterize each recording site's ability to detect neural units and LFPs instead of examining changes in single-unit waveform over time (Fraser and Schwartz, 2012). Future studies will evaluate the longitudinal stability of units at the electrode–tissue interface by combining optical and electrophysiological methods (Fraser and Schwartz, 2012; Kozai et al., 2012b).

It should be noted that anesthesia can influence the MU recording metrics. Therefore, they should not be evaluated alone, but rather evaluated with corresponding SU metrics. Of note is that the SU yield is much lower than the yield for detecting significant ($p < 0.05$) visually evoked neural activity. Despite the anesthesia (which was used to minimize movement related electrical artifact) the evoked unit yield, evoked SNFRR, SNLPR, evoked unit amplitude, and evoked LFP power show a much steadier decay than the corresponding SU metrics. This demonstrates that despite some variability that may be introduced from anesthesia level, this MU data provides a more stable metric and additional recording information beyond the corresponding SU metrics. In Fig. 14a–c, we show the combined electrode yield for being able to detect neural spike recording, SU and/or evoked MU (Tables S12 and S13).

As expected, the inability of an electrode site to detect a SU is not indicative of the inability of the recording site to detect useful neural information (Buzsaki et al., 2012; Flint et al., 2013; Fraser et al., 2009; Kozai et al., 2015a; Kozai et al., 2012a). Similarly, when compared to multiunit activity, LFPs have been shown to encode meaningful decoding features that are not found within the multiunit activity (Perel et al., 2013). While the two signals may be correlated, studies suggest that LFPs retain more signaling information than high frequency single neuronal activity alone (Perel et al., 2013). Therefore, LFP signals may supplement multiunit recordings even if LFPs have low SNR. Furthermore, specific neuroscience studies and applications examine specific recording signal type (SU, MU, or LFP) (Land et al., 2013a; Vazquez et al., 2013). For these studies, electrodes specifically designed to optimize application specific recordings (i.e. MU and LFP, instead of SU) may be more beneficial than using a single "one size fits all" recording electrode within a certain 1 kHz impedance range. It should be noted that the 10–100 Hz impedance correlate to LFP recording performance and while some similarities are shared with the 1 kHz impedance heat map, some distinct differences can also be observed. Therefore, the methods and metrics optimized here will be useful tools to assess the electrode property and performance for specific applications and research needs.

4.2. Stability of cortical layer depth after chronic implant

Another important observation is the depth of layer IV can shift over time (Fig. 7c and d). The bulk shift appears to be mostly in the first week and generally stabilizes by day 14 (Fig. 7e). This instability is also reflected in the electrode performance across multiple metrics (Fig. 6a–h).

In some animals, the depth of layer IV shifted deeper along the array. This might suggest that the electrode is being pushed out of the tissue, as suggested by device capture histology (Woolley et al., 2013). However, this is unlikely as the electrode was tightly anchored to the skull and bone screws with dental cement. In the case of the device-capture histology, it is likely that the tissue shrunk during the tissue fixation, and the sucrose based tissue dehydration and tissue clearing. During these tissue processing steps, the tissue volume shrinks, but the electrode does not. As a result, the probe anchored tissue stretches out along the electrode

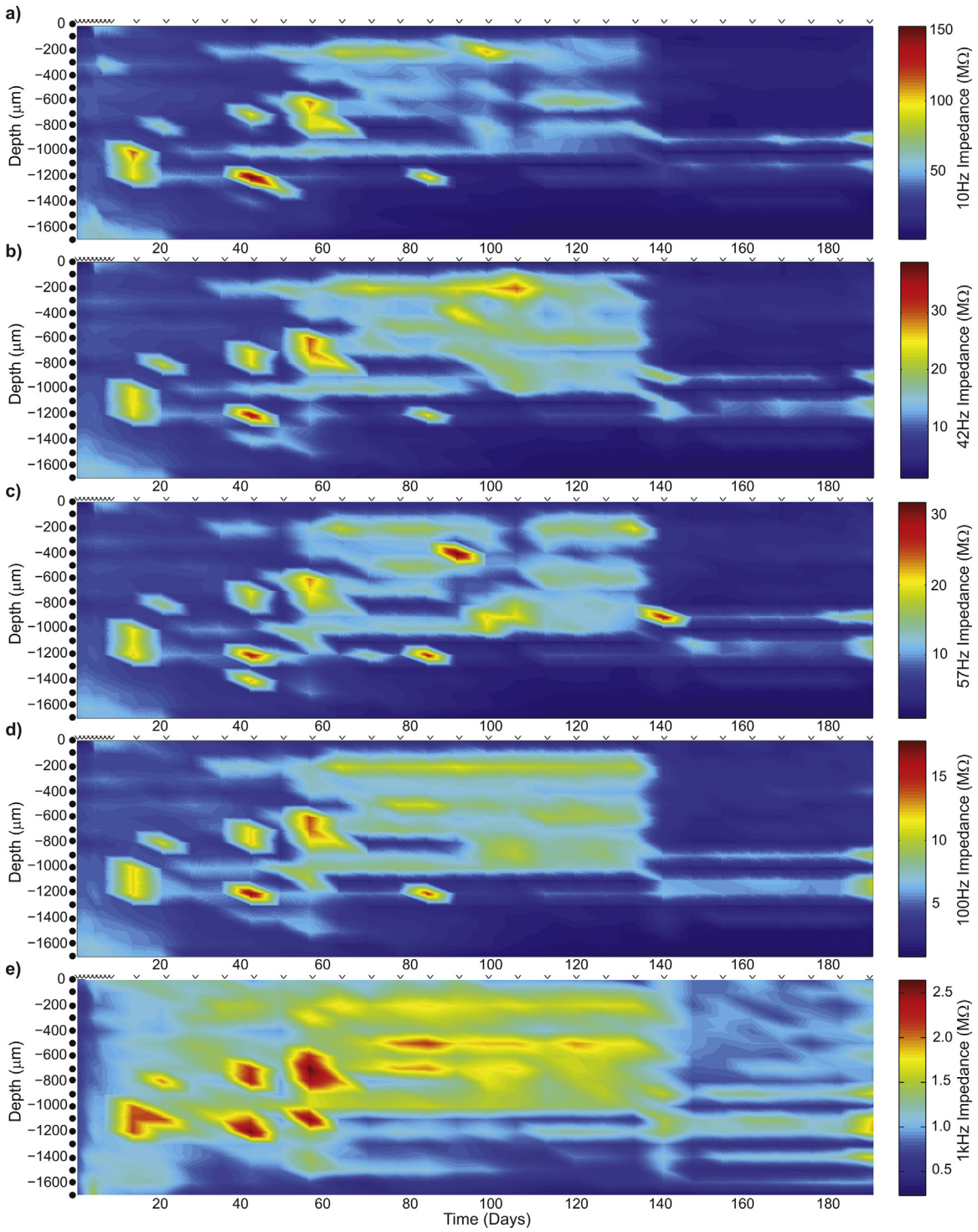

Fig. 13. LFP Range Impedance as a function of depth and time. (a) 10 Hz impedance. (b) 42 Hz impedance (frequency of peak average power of 'OFF' response). (c) 57 Hz impedance (frequency of peak average power of 'ON' response). (d) 100 Hz impedance. (e) 1 kHz impedance.

substrate, giving it the appearance that the probe is being pushed out. The more likely interpretation is that the tissue around the electrode is sinking. While previous studies have shown that thin skulled preparations have reduced glial activation compared to window-sealed open craniotomy, they have also shown that the tissue below the craniotomy does not sink over days (Xu et al., 2007). Instead, this tissue sinking is more frequently observed from infarcts following major vessel occlusion/thrombosis, and from intracortical hemorrhage (Shih et al., 2013).

While the cortex in vivo has been shown to be robust against microinfarcts from the occlusion or loss of oxygen perfusion in single capillaries/microvessels, microelectrode implants have been shown to occlude multiple adjacent microvessels in the immediate microenvironment of the electrode (Kozai et al., 2012b), and the loss of oxygen to a relatively large region of tissue may lead to ischemia, hypoxia, and/or infarcts (Boutin et al., 2001; Caso et al., 2006, 2007; Shih et al., 2013; Yamasaki et al., 1995; Zhang and Murphy, 2007). It should also be noted that solid planar probes with

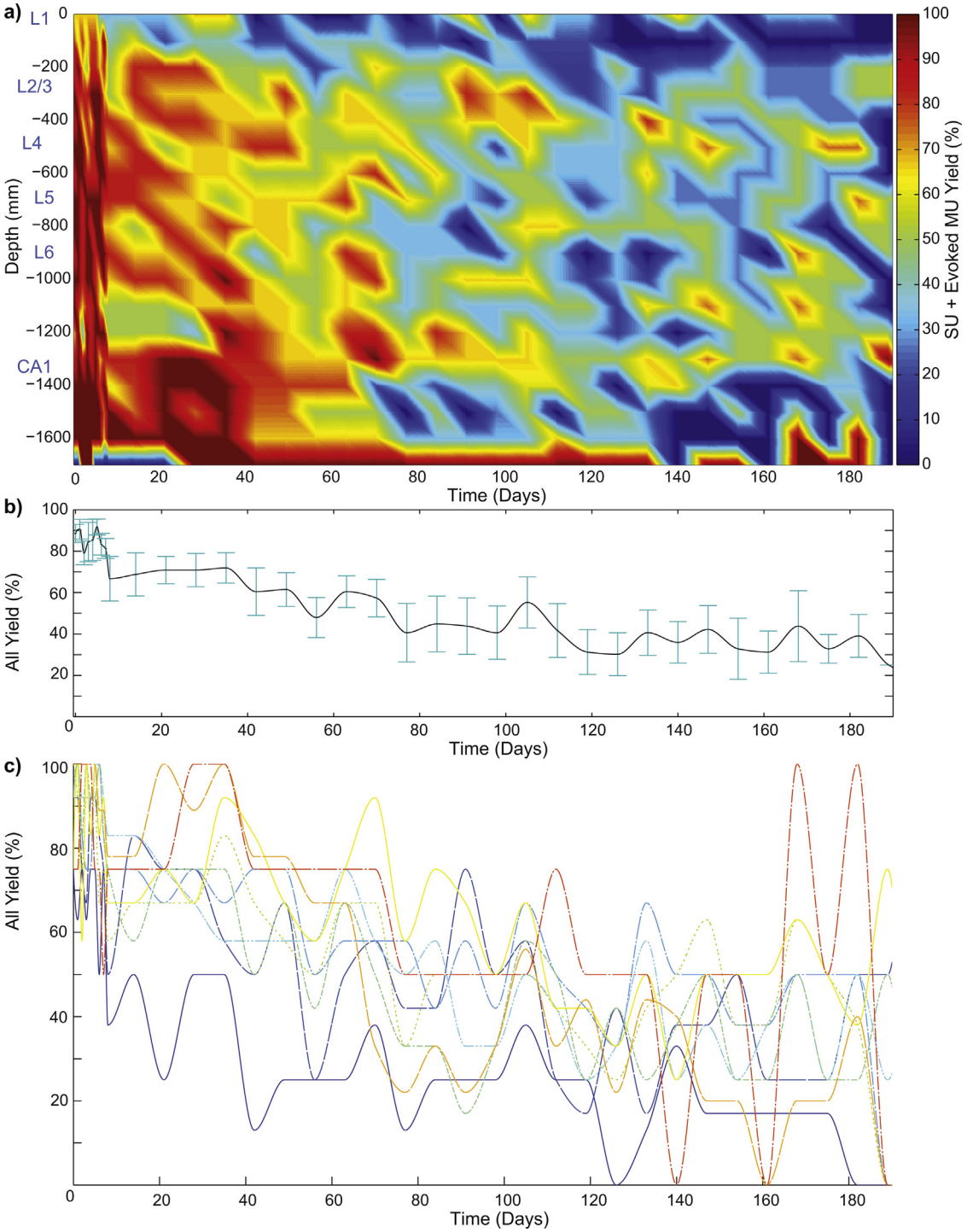

Fig. 14. Combined SU&MU yield over time for detecting sortable SUs and/or evoked multiunit activity: (a) across depth; (b) combined depths; and (c) individual depths: 0–100 (violet, solid), 200–300 (blue, dashed), 400–500 (navy, dash-dot), 600–700 (cyan, dash-dot-dot), 800–900 (green, dash-dash-dot), 1000–1100 (lime, dot-dot) 1200–1300 (yellow, solid), 1400–1500 (orange, dashed), 1600–1700 (red, dash-dot). (For interpretation of the references to color in this figure legend, the reader is referred to the web version of this article.)

lateral facing recording sites such as the ones used in this study may limit oxygen diffusion through the electrode surface, further contributing to an ischemic environment. This may be limited through open architecture lattice designs or sub-cellular sized designs. Lastly, it should be noted that the major neurovascular architecture is generally organized in the axis normal to the surface of the cortex (Kozai et al., 2010). Perpendicularly implanted electrodes that experience vascular injury in superficial layers may impact oxygen perfusion to deeper layers where the recording sites are located as observed with the occlusion of superficial major vessels(Shih et al., 2013).

As expected, when comparing the SU yield of the animal experiencing this depth decrease in layer IV, the initial unit yield decrease coincides with the decrease in layer IV's position (Fig. 6f). After the first week, the tissue depth partially recovers, and after a less than 1 week delay, the yield does the same. Because the

vasculature network was not pre-mapped before probe insertion, it is possible that major penetrating vessels were ruptured during insertion, despite avoiding major surface vessel by >49 μm (Kozai et al., 2010). The data suggest a period of stability, and then decay of SU yield, before the tissue dramatically sank and the yield fell to zero. Post-mortem examination of the brain showed decreased brain volume in both hemispheres, but no signs of infection or blood cell accumulation on the surface of the brain. Additional outlier subjects that show similar longitudinal patterns are needed to draw definitive correlations and conclusions.

In five of the eight examples, layer IV shifted toward a more superficial recording site on the first day following surgery. This suggests that the tissue dimpled around the electrode during the surgery then relaxed within 24 h. Electrode insertions were manually inserted at ~1 mm/s with a rigid stereotaxic guide. Reflections of the surgical lamp off of the surface of the cortex through an angled surgical scope showed no signs of dimpling.

As headcap cement hardens and polymerizes it slightly shrinks. In order to prevent this from breaking the brittle polysilica electrical traces in the electrode, the unimplanted region of the silicon probe was coated with soft silicone elastiomer. A droplet of silicone was carefully applied to the bottom edge of the print circuit board without bumping the probe, and allowed to drip down along the probe shank, and into the craniotomy. While the intention was to coat both sides of the probe simultaneously, navigating between the probe, bone screw, and ground/reference wires precluded simultaneous application of the silicone. It is possible that in some cases, the viscosity and surface tension of the silicone caused the silicon probe to deflect, causing some initial tissue compression that required one day equilibrating. This may highlight the underappreciated engineering problem associated with designing headcaps.

Lastly, a couple of examples showing continuous stable layer IV depth suggest that it is possible for implants to maintain a depth–stable interface, possibly by achieving specific surgical conditions, probe insertions, and probe fixation processes. Additional research should be aimed at understanding the cause for variability and improve reliability of the entire implantation and headcap processes. One example may be to map the 3D vascular network of the cortex prior to probe insertion in order to implant into regions of low vascular densities (Horton et al., 2013; Kozai et al., 2010).

4.3. Brain layer and electrode characteristics

The critical observation is that cortical layer impacts recording performance as well as electrode characteristics when comparing different probe designs (e.g. Michigan probe where electrodes are along the shanks and across multiple depth to Utah arrays where electrodes are at the same depth). Ignoring differences in cortical depth can dramatically bias the electrophysiological result. This bias can in turn limit the interpretations and conclusions on our understanding of the electrode–tissue interface and impede data driven technology design. One proposed solution is to only compare recording sites in the same layer in comparative studies. When comparing with bed of needle arrays with electrode sites that occupy a specific brain layer, this can be achieved by ignoring the recording performance of electrode sites that reside in different layers in linear arrays. Lastly, it is also important to consider the design of the electrodes for specific BCI applications and neuroscience research (e.g., Layer IV for sensory input and Layer V for motor output). These findings also point to new avenues of research toward elucidating the intrinsic anatomical, cellular, and molecular architecture of the brain and how its heterogeneity leads to differential tissue-implant interaction over time.

The mouse model is particularly advantageous for these studies due to the extensive genetic toolbox available for knocking out or knocking in specific genes, as well as tagging specific cell types for in vivo imaging (Kozai et al., 2014c; Kozai et al., 2012b). Furthermore, electrode arrays are expected to last longer in mice compared to larger animals due to reduced mechanical strain and material failure of the implants (Kozai et al., 2015a). Additionally, due to the reduced sizes of the mouse brain [V1: ~1 mm (Chen et al., 2014)] it is easier to record from multiple brain regions (e.g. cortex and hippocampus) compared to rats or non-human primates. The same array used in this study would not be able to span the entire cortex in rats [V1: 1.3–1.5 mm (Peters et al., 1985; Tyler et al., 1998)] or primates [V1: 1.6 mm (Tyler et al., 1998)]. However, for this reason it is important to carefully consider how the neuronal anatomical architecture of the mouse brain might be reflected in the electrophysiology performance (Fig. 15). The ability to sample from multiple regions may provide new insight on how distant brain regions are networked together. While such basic science research may not directly apply to technological translation, it provides the foundation for advancement of knowledge which leads to informed device design for specific neuroprosthetic and basic neuroscience research applications.

4.4. Summary

This study focused on the method of characterizing the layer dependent visually evoked chronic neural recording performance that takes advantage of large accessible cortical targets of rodent visual cortex while minimizing electrical and mechanical artifact. A multitude of analysis was provided to paint a comprehensive basic science level picture of the chronic electrophysiological performance landscape. Specifically, we established the methods for analyzing recording in a depth dependent manner, and defined and optimized novel metrics for quantifying evoked MU and LFP recording quality and stability. The key findings using these approaches are: (1) Evaluating electrode performance of resting state activity or resting state underestimates the number of neurons available for recording due to the presence of slow firing or quiescent neurons; (2) Depth of cortical layer IV can fluctuate in the first week following implantation, but generally stabilizes after 14 days (Fig. 7e); (3) There is a strong dependence between the biological layers of the cortex and underlying white matter on chronic SU and MU recording performance.

In addition, we demonstrated: (i) Evoking activity enables functional evaluation of MU activity, as well as some LFP activity, particularly in the Gamma range, (ii) Distinct 'ON' and 'OFF' unit and LFP activity can be observed, (iii) For 1 s 'ON' and 1 s 'OFF' stimulation under ~1.1% isofluorane anesthesia, paired *t*-test showed the greatest activity yield when comparing the number of threshold-crossing events 550 ms before and 550 ms after a 50 ms latency offset (the 50 ms delay compensates for the latency between the retina and the visual cortex), (iv) 'OFF' response shows sinks in layer II/III followed by layer V, (v) Large changes in layer IV depth coincided with parallel changes in SU yield, (vi) Evoked MU yield is greater than SU yield, (vii) The SNAR of SUs can increase after 11 weeks, (viii) SU yield, SNAR, and amplitude appear to be the greatest at more chronic implantation time in layer IV followed by layer II/III, (ix) layer V and stratum pyramidale have high acute and early chronic SU yield, SNAR, and amplitude, but rapidly fail over the first 11 weeks, (x) Very few SUs can be detected in neurite dominant layers (layer I, subcortical transcallosal white matter, and alveus), (xi) Inability to record SUs does not preclude the electrode from recording functional information (MU and LFP), (xii) Impedance and noise floor increase earlier from the tip (hippocampus) and the base (the surface of the cortex), (xiii) Evoked LFP activity is best quantified by comparing the peak evoked power after normalizing the to the resting state LFP, (xiv) Sharp increases in impedance may still be followed by impedance decreases over time, (xv) Using common average referencing reveals and strengthens LFP features

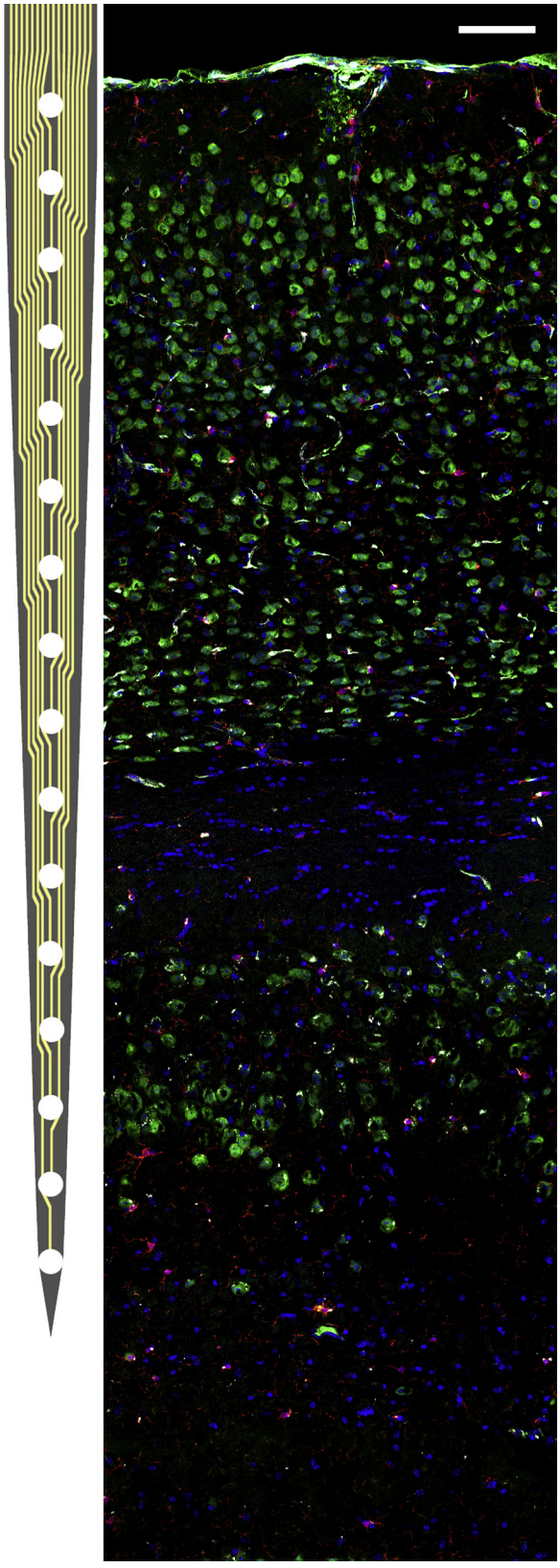

Fig. 15. Scaled model of A16-3mm-100-703 Michigan electrode next to layers of visual cortex and underlying layers of hippocampus. Neuronal nuclei (green), microglia (red), vascular structures (white), and all cell nuclei (blue). Scale bar indicates 100 μm. *Note*: Very few neurons are in Layer I and no neurons can be seen in the callosum and alveus. Also note: Tissue size can become distorted (shrink or stretch) during each tissue processing and staining steps, and may not exactly reflect the actual size in vivo. (For interpretation of the references to color in this figure legend, the reader is referred to the web version of this article.)

when compared to contralateral ECoG reference, (xvi) Neural recording voids in tissue may be from the natural architecture of the brain and not associated with injury, (xvii) LFP gamma band frequencies are similar along depth and across time in the visual cortex of mice, and (xviii) Evoked MU activity decreases more slowly than SUs across yield SNR, and amplitude.

5. Conclusion

Methods for quantifying evoked MU and LFP yield, signal quality, signal strength, signal steadiness were quantified and compared to corresponding SU recording characteristics. These findings also suggest that it is critical to consider the heterogeneity of the neural architecture when designing and evaluating new technology to current standards. Basic scientific understanding of the complex chronic electrode–tissue interface is necessary for directing treatments and technology development of next generation devices. This requires more complex evaluation tools and metrics to better understand the intimate details behind success and failure modes of chronically implanted electrodes for specific needs and applications. This work provides initial insight into elucidating this complex interaction through a more comprehensive characterization of the electrophysiological performance landscape.

Successful long-term implantable electrodes can accelerate the understanding behind the progression of neurodegenerative diseases and brain injury. Mice in particular are exceptional models because of the access to large genetic toolbox for knocking out and knocking in specific genes for various biological pathways. Additionally, new advances in molecular, biochemical, and biomimetic technology allows us to achieve seamless integration between biology and machine. As this goal becomes closer to reality, it may become necessary to evaluate interventions and treatment strategies not only for their ability to maintain neuronal survivability, but also neuronal health as it pertains to neurological function and networked activity.

Acknowledgement

The authors would like to thank Xia Li for assistance with histology. This work was financially supported by an NIH R01 (5R01NS062019-03) and The Pittsburgh Foundation. MAS was supported by R01 EY022928 from NIH. RMF was supported by NIH/NINDS R01s (5R01NS039324-15 and 5R01NS07748-04) and the David Scaife Family Foundation.

Appendix A. Supplementary data

Supplementary data associated with this article can be found, in the online version, at http://dx.doi.org/10.1016/j.jneumeth.2014.12.010.

References

Antolik J, Bednar JA. Development of maps of simple and complex cells in the primary visual cortex. Front Comput Neurosci 2011;5:17.
Azemi E, Gobbel GT, Cui XT. Seeding neural progenitor cells on silicon-based neural probes. J Neurosurg 2010;113:673–81.
Azemi E, Lagenaur CF, Cui XT. The surface immobilization of the neural adhesion molecule L1 on neural probes and its effect on neuronal density and gliosis at the probe/tissue interface. Biomaterials 2011;32:681–92.
Bair W, Cavanaugh JR, Smith MA, Movshon JA. The timing of response onset and offset in macaque visual neurons. J Neurosci 2002;22:3189–205.
Barrese JC, Rao N, Paroo K, Triebwasser C, Vargas-Irwin C, Franquemont L, Donoghue JP. Failure mode analysis of silicon-based intracortical microelectrode arrays in non-human primates. J Neural Eng 2013;10:066014.
Bjornsson CS, Oh SJ, Al-Kofahi YA, Lim YJ, Smith KL, Turner JN, De S, Roysam B, Shain W, Kim SJ. Effects of insertion conditions on tissue strain and vascular damage during neuroprosthetic device insertion. J Neural Eng 2006;3:196–207.

Bokil H, Andrews P, Kulkarni JE, Mehta S, Mitra PP. Chronux: a platform for analyzing neural signals. J Neurosci Methods 2010;192:146–51.

Boutin H, LeFeuvre RA, Horai R, Asano M, Iwakura Y, Rothwell NJ. Role of IL-1alpha and IL-1beta in ischemic brain damage. J Neurosci 2001;21:5528–34.

Brainard DH. The psychophysics toolbox. Spat Vis 1997;10:433–6.

Brodie SE, Knight BW, Ratliff F. The response of the Limulus retina to moving stimuli: a prediction by Fourier synthesis. J Gen Physiol 1978;72:129–66.

Burns SP, Xing D, Shapley RM. Comparisons of the dynamics of local field potential and multiunit activity signals in macaque visual cortex. J Neurosci 2010;30:13739–49.

Buzsaki G, Anastassiou CA, Koch C. The origin of extracellular fields and currents – EEG, ECoG, LFP and spikes. Nat Rev Neurosci 2012;13:407–20.

Caso JR, Lizasoain I, Lorenzo P, Moro MA, Leza JC. The role of tumor necrosis factor-alpha in stress-induced worsening of cerebral ischemia in rats. Neuroscience 2006;142:59–69.

Caso JR, Moro MA, Lorenzo P, Lizasoain I, Leza JC. Involvement of IL-1beta in acute stress-induced worsening of cerebral ischaemia in rats. Eur Neuropsychopharmacol 2007;17:600–7.

Chase SM, Kass RE, Schwartz AB. Behavioral and neural correlates of visuomotor adaptation observed through a brain–computer interface in primary motor cortex. J Neurophysiol 2012;108:624–44.

Chase SM, Schwartz AB, Kass RE. Bias, optimal linear estimation, and the differences between open-loop simulation and closed-loop performance of spiking-based brain–computer interface algorithms. Neural Netw 2009;22:1203–13.

Chen XJ, Rasch MJ, Chen G, Ye CQ, Wu S, Zhang XH. Binocular input coincidence mediates critical period plasticity in the mouse primary visual cortex. J Neurosci 2014;34:2940–55.

Chestek CA, Gilja V, Nuyujukian P, Foster JD, Fan JM, Kaufman MT, Churchland MM, Rivera-Alvidrez Z, Cunningham JP, Ryu SI, Shenoy KV. Long-term stability of neural prosthetic control signals from silicon cortical arrays in rhesus macaque motor cortex. J Neural Eng 2011;8:045005.

Collinger JL, Wodlinger B, Downey JE, Wang W, Tyler-Kabara EC, Weber DJ, McMorland AJ, Velliste M, Boninger ML, Schwartz AB. High-performance neuroprosthetic control by an individual with tetraplegia. Lancet 2012;381(9866):557–64.

Cornelissen FW, Peters EM, Palmer J. The eyelink toolbox: eye tracking with MATLAB and the psychophysics toolbox. Behav Res Methods Instrum Comput 2002;34:613–7.

Cui X, Hetke JF, Wiler JA, Anderson DJ, Martin DC. Electrochemical deposition and characterization of conducting polymer polypyrrole/PSS on multichannel neural probes. Sens Actuators A Phys 2001;93:8–18.

Cui X, Martin DC. Electrochemical deposition and characterization of poly (3,4-ethylenedioxythiophene) on neural microelectrode arrays. Sens Actuators B Chem 2003a;89:92–102.

Cui X, Martin DC. Fuzzy gold electrodes for lowering impedance and improving adhesion with electrodeposited conducting polymer films. Sens Actuators A Phys 2003b;103:384–94.

Dai J, Wang Y. Representation of surface luminance and contrast in primary visual cortex. Cereb Cortex 2012;22:776–87.

De Valois RL, Albrecht DG, Thorell LG. Spatial frequency selectivity of cells in macaque visual cortex. Vis Res 1982;22:545–59.

Fee MS, Mitra PP, Kleinfeld D. Automatic sorting of multiple unit neuronal signals in the presence of anisotropic and non-Gaussian variability. J Neurosci Methods 1996;69:175–88.

Flint RD, Wright ZA, Scheid MR, Slutzky MW. Long term, stable brain machine interface performance using local field potentials and multiunit spikes. J Neural Eng 2013;10:056005.

Foster KH, Gaska JP, Nagler M, Pollen DA. Spatial and temporal frequency selectivity of neurones in visual cortical areas V1 and V2 of the macaque monkey. J Physiol 1985;365:331–63.

Fraser GW, Chase SM, Whitford A, Schwartz AB. Control of a brain–computer interface without spike sorting. J Neural Eng 2009;6:055004.

Fraser GW, Schwartz AB. Recording from the same neurons chronically in motor cortex. J Neurophysiol 2012;107:1970–8.

Gage GJ, Stoetzner CR, Wiltschko AB, Berke JD. Selective activation of striatal fast-spiking interneurons during choice execution. Neuron 2010;67:466–79.

Ganguly K, Carmena JM. Emergence of a stable cortical map for neuroprosthetic control. PLoS Biol 2009;7:e1000153.

Gao E, DeAngelis GC, Burkhalter A. Parallel input channels to mouse primary visual cortex. J Neurosci 2010;30:5912–26.

Gavornik JP, Bear MF. Learned spatiotemporal sequence recognition and prediction in primary visual cortex. Nat Neurosci 2014;17:732–7.

Gilgunn PJ, Khilwani R, Kozai TDY, Weber DJ, Cui XT, Erdos G, Ozdoganlar OB, Fedder GK. An ultra-compliant, scalable neural probes with molded biodissolvable delivery vehicle. In: 2012 IEEE 25th international conference on micro electro mechanical systems (MEMS), vol. 2012; 2012. p. 56–9.

Goncalves JT, Anstey JE, Golshani P, Portera-Cailliau C. Circuit level defects in the developing neocortex of Fragile X mice. Nat Neurosci 2013;16:903–9.

Guitchounts G, Markowitz JE, Liberti WA, Gardner TJ. A carbon-fiber electrode array for long-term neural recording. J Neural Eng 2013;10:046016.

Haider B, Hausser M, Carandini M. Inhibition dominates sensory responses in the awake cortex. Nature 2013;493:97–100.

Harding GF, Fylan F. Two visual mechanisms of photosensitivity. Epilepsia 1999;40:1446–51.

Harris JP, Capadona JR, Miller RH, Healy BC, Shanmuganathan K, Rowan SJ, Weder C, Tyler DJ. Mechanically adaptive intracortical implants improve the proximity of neuronal cell bodies. J Neural Eng 2011;8:066011.

Harris S, Jones M, Zheng Y, Berwick J. Does neural input or processing play a greater role in the magnitude of neuroimaging signals? Front Neuroenerg 2010;2.

Henze DA, Borhegyi Z, Csicsvari J, Mamiya A, Harris KD, Buzsaki G. Intracellular features predicted by extracellular recordings in the hippocampus in vivo. J Neurophysiol 2000;84:390–400.

Hochberg LR, Bacher D, Jarosiewicz B, Masse NY, Simeral JD, Vogel J, Haddadin S, Liu J, Cash SS, van der Smagt P, Donoghue JP. Reach and grasp by people with tetraplegia using a neurally controlled robotic arm. Nature 2012;485:372–5.

Horton NG, Wang K, Kobat D, Clark CG, Wise FW, Schaffer CB, Xu C. In vivo three-photon microscopy of subcortical structures within an intact mouse brain. Nat Photon 2013;7:205–9.

Hudson AE, Calderon DP, Pfaff DW, Proekt A. Recovery of consciousness is mediated by a network of discrete metastable activity states. Proc Natl Acad Sci U S A 2014.

Jarosiewicz B, Chase SM, Fraser GW, Velliste M, Kass RE, Schwartz AB. Functional network reorganization during learning in a brain–computer interface paradigm. Proc Natl Acad Sci U S A 2008;105:19486–91.

Jeyabalaratnam J, Bharmauria V, Bachatene L, Cattan S, Angers A, Molotchnikoff S. Adaptation shifts preferred orientation of tuning curve in the mouse visual cortex. PLoS ONE 2013;8:e64294.

Jia X, Smith MA, Kohn A. Stimulus selectivity and spatial coherence of gamma components of the local field potential. J Neurosci 2011;31:9390–403.

Jin J, Wang Y, Swadlow HA, Alonso JM. Population receptive fields of ON and OFF thalamic inputs to an orientation column in visual cortex. Nat Neurosci 2011;14:232–8.

Johnson MD, Kao OE, Kipke DR. Spatiotemporal pH dynamics following insertion of neural microelectrode arrays. J Neurosci Methods 2007;160:276–87.

Karumbaiah L, Saxena T, Carlson D, Patil K, Patkar R, Gaupp EA, Betancur M, Stanley GB, Carin L, Bellamkonda RV. Relationship between intracortical electrode design and chronic recording function. Biomaterials 2013;34:8061–74.

Kipke DR, Shain W, Buzsaki G, Fetz E, Henderson JM, Hetke JF, Schalk G. Advanced neurotechnologies for chronic neural interfaces: new horizons and clinical opportunities. J Neurosci 2008;28:11830–8.

Kleiner M, Brainard DH, Pelli DG. What's new in psychtoolbox-3? Perception 2007;36, ECVP Abstract Supplement.

Kolarcik CL, Bourbeau D, Azemi E, Rost E, Zhang L, Lagenaur CF, Weber DJ, Cui XT. In vivo effects of L1 coating on inflammation and neuronal health at the electrode–tissue interface in rat spinal cord and dorsal root ganglion. Acta Biomater 2012;8:3561–75.

Kolarcik CL, Catt K, Rost E, Albercht IN, Bourbeau D, Du Z, Kozai TDY, Luo X, Weber DJ, Cui XT. Evaluation of poly(3,4-ethylenedioxythiophene)/carbon nanotube neural electrode coatings for stimulation in the dorsal root ganglion. J Neural Eng 2014;12:016008.

Kozai TDY, Alba N, Zhang H, Kotov N, Gaunt R, Cui X. Nanostructured coatings for improved charge delivery to neurons. In: Vittorio MD, Martiradonna L, Assad J, editors. Nanotechnology and neuroscience: nano-electronic, photonic and mechanical neuronal interfacing. New York, NY: Springer New York; 2014a. p. 71–134.

Kozai TDY, Catt K, Li X, Gugel ZV, Olafsson VT, Vazquez AL, Cui XT. Mechanical failure modes of chronically implanted planar silicon-based neural probes for laminar recording. Biomaterials 2015a;37:25–39.

Kozai TDY, Gugel Z, Li X, Gilgunn PJ, Khilwani R, Ozdoganlar OB, Fedder GK, Weber DJ, Cui XT. Chronic tissue response to carboxymethyl cellulose based dissolvable insertion needle for ultra-small neural probes. Biomaterials 2014b;35:9255–68.

Kozai TDY, Jaquins-Gerstl AS, Vazquez AL, Michael AC, Cui XT. Brain tissue responses to neural implants impact signal sensitivity and intervention strategies. ACS Chem Neurosci 2015b., http://dx.doi.org/10.1021/cn500256e (in press).

Kozai TDY, Kipke DR. Insertion shuttle with carboxyl terminated self-assembled monolayer coatings for implanting flexible polymer neural probes in the brain. J Neurosci Methods 2009;184:199–205.

Kozai TDY, Langhals NB, Patel PR, Deng X, Zhang H, Smith KL, Lahann J, Kotov NA, Kipke DR. Ultrasmall implantable composite microelectrodes with bioactive surfaces for chronic neural interfaces. Nat Mater 2012a;11:1065–73.

Kozai TDY, Li X, Bodily LM, Caparosa EM, Zenonos GA, Carlisle DL, Friedlander RM, Cui XT. Effects of caspase-1 knockout on chronic neural recording quality and longevity: insight into cellular and molecular mechanisms of the reactive tissue response. Biomaterials 2014c;35:9620–34.

Kozai TDY, Marzullo TC, Hooi F, Langhals NB, Majewska AK, Brown EB, Kipke DR. Reduction of neurovascular damage resulting from microelectrode insertion into the cerebral cortex using in vivo two-photon mapping. J Neural Eng 2010;7:046011.

Kozai TDY, Vazquez AL, Weaver CL, Kim SG, Cui XT. In vivo two photon microscopy reveals immediate microglial reaction to implantation of microelectrode through extension of processes. J Neural Eng 2012b;9:066001.

Kuhlman SJ, Tring E, Trachtenberg JT. Fast-spiking interneurons have an initial orientation bias that is lost with vision. Nat Neurosci 2011;14:1121–3.

Land R, Engler G, Kral A, Engel AK. Response properties of local field potentials and multiunit activity in the mouse visual cortex. Neuroscience 2013a.

Land R, Engler G, Kral A, Engel AK. Response properties of local field potentials and multiunit activity in the mouse visual cortex. Neuroscience 2013b;254:141–51.

Lennie P. The physiological basis of variations in visual latency. Vis Res 1981;21:815–24.

Ludwig KA, Miriani RM, Langhals NB, Joseph MD, Anderson DJ, Kipke DR. Using a common average reference to improve cortical neuron recordings from microelectrode arrays. J Neurophysiol 2009;101:1679–89.

Luo X, Matranga C, Tan S, Alba N, Cui XT. Carbon nanotube nanoreservior for controlled release of anti-inflammatory dexamethasone. Biomaterials 2011;32:6316–23.
Marshall WH, Talbot SA, Ades HW. Cortical response of the anesthetized cat to gross photic and electrical afferent stimulation. J Neurophysiol 1943;6:1–15.
McGuire BA, Hornung JP, Gilbert CD, Wiesel TN. Patterns of synaptic input to layer 4 of cat striate cortex. J Neurosci 1984;4:3021–33.
Mitzdorf U, Singer W. Prominent excitatory pathways in the cat visual cortex (A 17 and A 18): a current source density analysis of electrically evoked potentials. Exp Brain Res 1978;33:371–94.
Mukamel EA, Pirondini E, Babadi B, Wong KF, Pierce ET, Harrell PG, Walsh JL, Salazar-Gomez AF, Cash SS, Eskandar EN, Weiner VS, Brown EN, Purdon PL. A transition in brain state during propofol-induced unconsciousness. J Neurosci 2014;34:839–45.
Murray SO, Kersten D, Olshausen BA, Schrater P, Woods DL. Shape perception reduces activity in human primary visual cortex. Proc Natl Acad Sci U S A 2002;99:15164–9.
Niell CM, Stryker MP. Highly selective receptive fields in mouse visual cortex. J Neurosci 2008;28:7520–36.
Olsen SR, Bortone DS, Adesnik H, Scanziani M. Gain control by layer six in cortical circuits of vision. Nature 2012;483:47–52.
Pelli DG. The videotoolbox software for visual psychophysics: transforming numbers into movies. Spat Vis 1997;10:437–42.
Perel S, Sadtler PT, Godlove JM, Ryu SI, Wang W, Batista AP, Chase SM. Direction and speed tuning of motor-cortex multi-unit activity and local field potentials during reaching movements. Conf Proc IEEE Eng Med Biol Soc 2013;2013:299–302.
Peters A, Kara DA, Harriman KM. The neuronal composition of area 17 of rat visual cortex III. Numerical considerations. J Comp Neurol 1985;238:263–74.
Potter KA, Buck AC, Self WK, Callanan ME, Sunil S, Capadona JR. The effect of resveratrol on neurodegeneration and blood brain barrier stability surrounding intracortical microelectrodes. Biomaterials 2013;34:7001–15.
Potter KA, Buck AC, Self WK, Capadona JR. Stab injury and device implantation within the brain results in inversely multiphasic neuroinflammatory and neurodegenerative responses. J Neural Eng 2012;9:046020.
Purcell EK, Seymour JP, Yandamuri S, Kipke DR. In vivo evaluation of a neural stem cell-seeded prosthesis. J Neural Eng 2009;6:026005.
Raiguel SE, Lagae L, Gulyas B, Orban GA. Response latencies of visual cells in macaque areas V1, V2 and V5. Brain Res 1989;493:155–9.
Richardson AG, Borghi T, Bizzi E. Activity of the same motor cortex neurons during repeated experience with perturbed movement dynamics. J Neurophysiol 2012;107:3144–54.
Rousche PJ, Normann RA. Chronic recording capability of the Utah Intracortical Electrode Array in cat sensory cortex. J Neurosci Methods 1998;82:1–15.
Sakatani T, Isa T. PC-based high-speed video-oculography for measuring rapid eye movements in mice. Neurosci Res 2004;49:123–31.
Sawyer AJ, Kyriakides TR. Nanoparticle-based evaluation of blood-brain barrier leakage during the foreign body response. J Neural Eng 2013;10:016013.
Saxena T, Karumbaiah L, Gaupp EA, Patkar R, Patil K, Betancur M, Stanley GB, Bellamkonda RV. The impact of chronic blood–brain barrier breach on intracortical electrode function. Biomaterials 2013;34:4703–13.
Schmolesky MT, Wang Y, Hanes DP, Thompson KG, Leutgeb S, Schall JD, Leventhal AG. Signal timing across the macaque visual system. J Neurophysiol 1998;79:3272–8.
Scott BB, Gardner T, Ji N, Fee MS, Lois C. Wandering neuronal migration in the postnatal vertebrate forebrain. J Neurosci 2012;32:1436–46.
Sellers KK, Bennett DV, Hutt A, Frohlich F. Anesthesia differentially modulates spontaneous network dynamics by cortical area and layer. J Neurophysiol 2013;110:2739–51.
Shih AY, Blinder P, Tsai PS, Friedman B, Stanley G, Lyden PD, Kleinfeld D. The smallest stroke: occlusion of one penetrating vessel leads to infarction and a cognitive deficit. Nat Neurosci 2013;16:55–63.
Shoham SNS. The theory of central nervous system recording. In: Horch KWDG, editor. Neuroprosthetics: theory and practice. Singapore: World Scientific Publishing; 2003. p. 448–65.
Shoham S, O'Connor DH, Segev R. How silent is the brain: is there a dark matter problem in neuroscience. J Comp Physiol A 2006;192:777–84.
Simeral JD, Kim SP, Black MJ, Donoghue JP, Hochberg LR. Neural control of cursor trajectory and click by a human with tetraplegia 1000 days after implant of an intracortical microelectrode array. J Neural Eng 2011;8:025027.
Smith MA, Jia X, Zandvakili A, Kohn A. Laminar dependence of neuronal correlations in visual cortex. J Neurophysiol 2013;109:940–7.
Spaak E, Bonnefond M, Maier A, Leopold DA, Jensen O. Layer-specific entrainment of gamma-band neural activity by the alpha rhythm in monkey visual cortex. Curr Biol 2012;22:2313–8.
Stensaas SS, Stensaas LJ. The reaction of the cerebral cortex to chronically implanted plastic needles. Acta Neuropathol 1976;35:187–203.
Stoelzel CR, Bereshpolova Y, Swadlow HA. Stability of thalamocortical synaptic transmission across awake brain states. J Neurosci 2009;29:6851–9.
Stoetzner CR, Pettibone JR, Berke JD. State-dependent plasticity of the corticostriatal pathway. Neuroscience 2010;165:1013–8.
Tyler CJ, Dunlop SA, Lund RD, Harman AM, Dann JF, Beazley LD, Lund JS. Anatomical comparison of the macaque and marsupial visual cortex: common features that may reflect retention of essential cortical elements. J Comp Neurol 1998;400:449–68.
Vazquez AL, Fukuda M, Crowley JC, Kim SG. Neural and hemodynamic responses elicited by forelimb- and photo-stimulation in channelrhodopsin-2 mice: insights into the hemodynamic point spread function. Cereb Cortex 2013.
Vetter P, Smith FW, Muckli L. Decoding sound and imagery content in early visual cortex. Curr Biol 2014.
Vogels R, Orban GA. Activity of inferior temporal neurons during orientation discrimination with successively presented gratings. J Neurophysiol 1994;71:1428–51.
Ward MP, Rajdev P, Ellison C, Irazoqui PP. Toward a comparison of microelectrodes for acute and chronic recordings. Brain Res 2009;1282:183–200.
Williams JC, Rennaker RL, Kipke DR. Long-term neural recording characteristics of wire microelectrode arrays implanted in cerebral cortex. Brain Res Brain Res Protoc 1999;4:303–13.
Winslow BD, Christensen MB, Yang WK, Solzbacher F, Tresco PA. A comparison of the tissue response to chronically implanted Parylene-C-coated and uncoated planar silicon microelectrode arrays in rat cortex. Biomaterials; 2010.
Woolley AJ, Desai HA, Otto KJ. Chronic intracortical microelectrode arrays induce non-uniform, depth-related tissue responses. J Neural Eng 2013;10:026007.
Xing D, Yeh CI, Burns S, Shapley RM. Laminar analysis of visually evoked activity in the primary visual cortex. Proc Natl Acad Sci U S A 2012;109:13871–6.
Xu HT, Pan F, Yang G, Gan WB. Choice of cranial window type for in vivo imaging affects dendritic spine turnover in the cortex. Nat Neurosci 2007;10:549–51.
Yamasaki Y, Matsuura N, Shozuhara H, Onodera H, Itoyama Y, Kogure K. Interleukin-1 as a pathogenetic mediator of ischemic brain damage in rats. Stroke 1995;26:676–80, discussion 81.
Yazdan-Shahmorad A, Lehmkuhle MJ, Gage GJ, Marzullo TC, Parikh H, Miriani RM, Kipke DR. Estimation of electrode location in a rat motor cortex by laminar analysis of electrophysiology and intracortical electrical stimulation. J Neural Eng 2011;8:046018.
Zhang SX, Murphy TH. Imaging the impact of cortical microcirculation on synaptic structure and sensory-evoked hemodynamic responses in vivo. PLoS Biol 2007;5:1152–67.
Zhong Y, Bellamkonda RV. Controlled release of anti-inflammatory agent [alpha]-MSH from neural implants. J Control Release 2005;106:309–18.